Molecular Cell

Resource

Synthetic Lethal and Resistance Interactions with BET Bromodomain Inhibitors in Triple-Negative Breast Cancer

Graphical Abstract

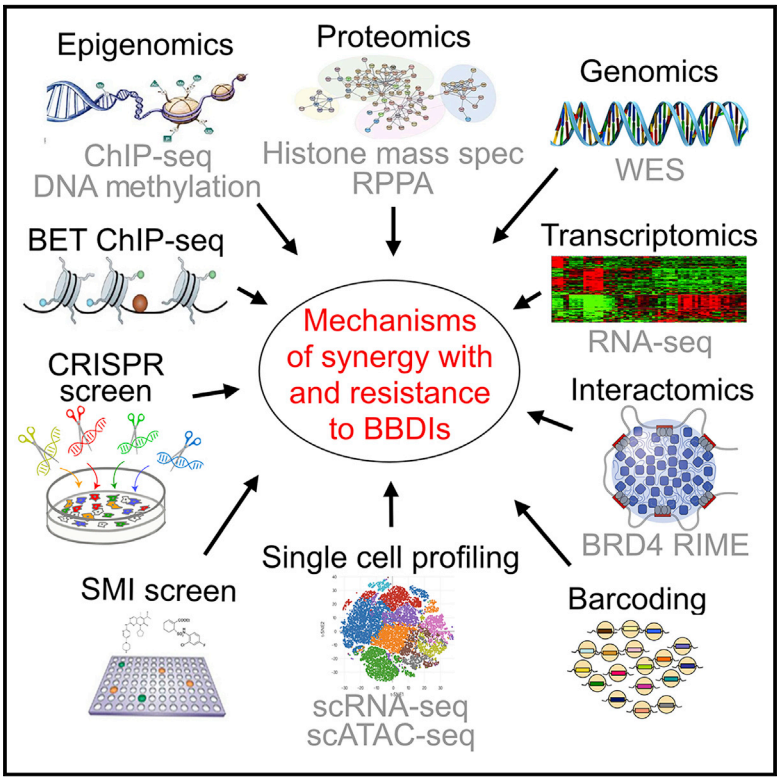

Authors

Shaokun Shu, Hua-Jun Wu, Jennifer Y. Ge, ..., James Bradner, Franziska Michor, Kornelia Polyak

Correspondence

michor@jimmy.harvard.edu (F.M.), kornelia_polyak@dfci.harvard.edu (K.P.)

In Brief

Shu et al. conducted integrated comprehensive molecular profiling and functional screens to identify synthetic lethal and resistance interactions with BET bromodomain inhibitors. CDK4 and BRD2 are top synthetic lethal hits, whereas deletion of BRD7 leads to resistance because of activation of genes suppressed by BET inhibitors in sensitive cells.

Highlights

- Synthetic lethal and resistance interactions with BET inhibitors in TNBC
- Multiple independent unbiased screens identify the same genes and pathways
- CDK4/6 inhibitors and paclitaxel have top synergies with BET bromodomain inhibitors
- Deletion of SNF/SWI complex components leads to BET inhibitor resistance

Shu et al., 2020, Molecular Cell *78*, 1096–1113
June 18, 2020
https://doi.org/10.1016/j.molcel.2020.04.027

CellPress

CellPress

Molecular Cell

Resource

Synthetic Lethal and Resistance Interactions with BET Bromodomain Inhibitors in Triple-Negative Breast Cancer

Shaokun Shu,[1,7,18,19] Hua-Jun Wu,[2,11,12,18] Jennifer Y. Ge,[1,2,13] Rhamy Zeid,[1,20] Isaac S. Harris,[8,14] Bojana Jovanović,[1,7,16] Katherine Murphy,[1] Binbin Wang,[2,21] Xintao Qiu,[1,5] Jennifer E. Endress,[8,14] Jaime Reyes,[1] Klothilda Lim,[1,5] Alba Font-Tello,[1,5] Sudeepa Syamala,[1,5] Tengfei Xiao,[2] Chandra Sekhar Reddy Chilamakuri,[15] Evangelia K. Papachristou,[15] Clive D'Santos,[15] Jayati Anand,[1] Kunihiko Hinohara,[1,7] Wei Li,[2,11,22] Thomas O. McDonald,[2,6,11,12] Adrienne Luoma,[3,9] Rebecca J. Modiste,[17] Quang-De Nguyen,[17] Brittany Michel,[4] Paloma Cejas,[1,5] Cigall Kadoch,[4,10,16] Jacob D. Jaffe,[16] Kai W. Wucherpfennig,[3,9] Jun Qi,[1] X. Shirley Liu,[2,5,11] Henry Long,[1,5] Myles Brown,[1,5,7,14] Jason S. Carroll,[15] Joan S. Brugge,[8,14] James Bradner,[1,7,23] Franziska Michor,[2,6,11,12,14,16,*] and Kornelia Polyak[1,5,6,7,14,16,24,*]

[1]Department of Medical Oncology, Dana-Farber Cancer Institute, Boston, MA 02215, USA
[2]Department of Data Sciences, Dana-Farber Cancer Institute, Boston, MA 02215, USA
[3]Department of Cancer Immunology and Virology, Dana-Farber Cancer Institute, Boston, MA 02215, USA
[4]Department of Pediatric Oncology, Dana-Farber Cancer Institute, Boston, MA 02215, USA
[5]Center for Functional Cancer Epigenetics, Dana-Farber Cancer Institute, Boston, MA 02215, USA
[6]Center for Cancer Evolution, Dana-Farber Cancer Institute, Boston, MA 02215, USA
[7]Department of Medicine, Harvard Medical School, Boston, MA 02115, USA
[8]Department of Cell Biology, Harvard Medical School, Boston, MA 02115, USA
[9]Department of Microbiology and Immunobiology, Harvard Medical School, Boston, MA 02115, USA
[10]Department of Biological Chemistry and Molecular Pharmacology, Harvard Medical School, Boston, MA 02115, USA
[11]Harvard T. H. Chan School of Public Health, Boston, MA 02115, USA
[12]Department of Stem Cell and Regenerative Biology, Harvard University, Cambridge, MA 02138, USA
[13]Harvard-MIT Division of Health Sciences and Technology, Harvard Medical School, Boston, MA 02215, USA
[14]Ludwig Center at Harvard, Boston, MA 02115, USA
[15]Cancer Research UK Cambridge Institute, University of Cambridge, Robinson Way, Cambridge CB2 0RE, UK
[16]The Eli and Edythe L. Broad Institute, Cambridge, MA 02142, USA
[17]Lurie Family Imaging Center, Center for Biomedical Imaging in Oncology, Dana-Farber Cancer Institute, Boston, MA 02215, USA
[18]These authors contributed equally
[19]Present address: Peking University Cancer Hospital and Institute, Beijing 100142, China
[20]Present address: C4 Therapeutics, Inc., Watertown, MA 02472, USA
[21]Present address: Shanghai Pulmonary Hospital, Tongji University, Shanghai 200092, China
[22]Present address: Children's National Medical Center, Washington, DC 20010, USA
[23]Present address: Novartis Institutes for BioMedical Research, Cambridge, MA 02139, USA
[24]Lead Contact
*Correspondence: michor@jimmy.harvard.edu (F.M.), kornelia_polyak@dfci.harvard.edu (K.P.)
https://doi.org/10.1016/j.molcel.2020.04.027

SUMMARY

BET bromodomain inhibitors (BBDIs) are candidate therapeutic agents for triple-negative breast cancer (TNBC) and other cancer types, but inherent and acquired resistance to BBDIs limits their potential clinical use. Using CRISPR and small-molecule inhibitor screens combined with comprehensive molecular profiling of BBDI response and resistance, we identified synthetic lethal interactions with BBDIs and genes that, when deleted, confer resistance. We observed synergy with regulators of cell cycle progression, YAP, AXL, and SRC signaling, and chemotherapeutic agents. We also uncovered functional similarities and differences among BRD2, BRD4, and BRD7. Although deletion of BRD2 enhances sensitivity to BBDIs, BRD7 loss leads to gain of TEAD-YAP chromatin binding and luminal features associated with BBDI resistance. Single-cell RNA-seq, ATAC-seq, and cellular barcoding analysis of BBDI responses in sensitive and resistant cell lines highlight significant heterogeneity among samples and demonstrate that BBDI resistance can be pre-existing or acquired.

INTRODUCTION

Triple-negative breast cancer (TNBC) is characterized by the absence of estrogen receptor (ER), progesterone receptor (PR) expression, and human epidermal growth factor receptor 2 (HER2). Only about 30%–40% of TNBC patients respond well to chemotherapy, and even though a subset of TNBC express PD-L1 and benefit from immunotherapy (Garrido-Castro et al., 2019), novel therapeutic options are needed for the majority of patients with advanced disease. TNBC genome sequencing studies have failed to identify recurrently mutated therapeutic targets and revealed extensive inter- and intratumor heterogeneity (Garrido-Castro et al., 2019). This heterogeneity suggests that multiple new therapeutic approaches involving combinations of agents are required for effective treatment of TNBC patients.

Bromo- and extra-terminal domain (BBD) proteins (e.g., BRD2–BRD4) are emerging therapeutic targets in TNBC. Directly acting BBD inhibitors (BBDIs), including JQ1 (Filippakopoulos et al., 2010), utilize acetyl-lysine-competitive binding to displace BBD proteins from chromatin, resulting in selective transcriptional responses and anti-proliferative efficacy (Delmore et al., 2011; Filippakopoulos et al., 2010; Puissant et al., 2013). The selectivity of BBD inhibition arises from localization of BBDs to super-enhancers (SEs) that regulate cell-specifying and oncogenic transcriptional programs (Chapuy et al., 2013; Hnisz et al., 2013; Lovén et al., 2013; Whyte et al., 2013), producing anti-tumor effects in preclinical models and in clinical trials (O'Dwyer et al., 2016; Shapiro et al., 2015; Shu and Polyak, 2016). We previously identified BBDIs as potential therapeutic agents in TNBC (Shu et al., 2016) but also found that acquired resistance emerges early, necessitating development of rational combinations. Thus, to identify synthetic lethal and resistance interactions with BBDIs and to decipher the underlying mechanisms, we performed unbiased comprehensive functional screens combined with multi-omics profiling using matched pairs of BBDI-sensitive and acquired-resistant TNBC cell lines.

RESULTS

CRISPR Screens to Uncover Synthetic Lethal and Resistance Interactions with JQ1

To identify synthetic lethal targets and mechanisms of resistance to BBDIs, we performed a genome-wide CRISPR-Cas9 knockout screen in the TNBC cell lines SUM159 and SUM149, treated with JQ1 or DMSO, and in their BBDI-resistant derivatives SUM159R and SUM149R, which we generated previously (Shu et al., 2016). Cells with knockout of known essential genes, including ribosomal genes, were strongly depleted in both treatments (Figure S1A), confirming the quality of the data. Across both parental cell lines, single guide RNAs (sgRNAs) that became specifically depleted after JQ1 treatment included those targeting G1-S cell cycle progression (*CDK4* and *SKP2*), oncogenic transcriptional regulators (*BRD2*, *EP300*, *CREBBP*, and *NELFB*), and DNA damage repair (*PRKDC*), indicating that these pathways became more essential under bromodomain inhibition and are synergistic with JQ1 (Figures 1A and 1B; Table S1). Conversely, sgRNAs that targeted G1-S cell cycle inhibitors (*CDKN1A*) and tumor-suppressive transcriptional regulators (*ARID1A* and *TCEB3*) were enriched, indicating that they contribute to JQ1 resistance. TCEB3 interacts with BRD3, and JQ1 treatment increases its binding (Lambert et al., 2019), which may explain why it was a hit in our screen. Other cell cycle regulators (*MYC* and *CCND1*) and transcriptional activators, including Mediator complex components (*MED23*, *MED24*, and *MED30*), were synergistic hits in SUM159 cells, whereas cell cycle- and transcription-related tumor suppressors (*RB1* and *BRD7*) were resistance hits. Many of our CRISPR hits (e.g., *CDK4* and *EP300*) are also dependencies in cell lines that depend on BRD4 in the Dependency Map (DepMap) data (Tsherniak et al., 2017; Figures S1B and S1C).

In SUM149 cells, deletion of *CSNK2B*, a subunit of CK2 that phosphorylates and stabilizes BRD4 (Wu et al., 2013), was synergistic with JQ1, whereas deletion of genes known to function in ubiquitination of BRD4 (*SPOP* and *CUL3*) and promote proteasomal degradation (Dai et al., 2017; Janouskova et al., 2017; Zhang et al., 2017) made cells more resistant (Figure 1A). Proteasomal subunits were also synergistic hits in SUM159 and SUM149 cells, and ubiquitin-proteasomal proteolysis was the top enriched process network in SUM149 cells (Figure S1D). These data are consistent with our prior finding that CK2-mediated phosphorylation and stabilization of BRD4 on chromatin is one of the mechanisms of acquired BBDI resistance (Shu et al., 2016).

In BBDI-resistant SUM159R and SUM149R cells, genes involved in transcription by RNA polymerase II were enriched among the top synergistic hits (Figure 1A). Moreover, RNA polymerase II complex regulation was the most significantly enriched pathway among synergistic genes in both resistant cell lines, implying that BBDI resistance still relies on BRD4/RNA polymerase II complex function (Figures 1C and S1D). This observation is consistent with our prior data demonstrating that BBDI-resistant cells still depend on BRD4 (Shu et al., 2016). Notably, *CDK4* and *BRD2* were top synergy hits in all four cell lines, suggesting that their deletion not only sensitizes cells to BBDIs but also overcomes acquired BBDI resistance (Figures 1A and 1B).

Integration of CRISPR Hits and Molecular Profiles

To explore mechanisms by which the CRISPR screen hits exert their function, we analyzed genetic alterations, gene expression, DNA methylation, histone and protein modifications, and the BRD4 interactome of parental and BBDI-resistant cells before and after JQ1 treatment. Although we identified several mutations specific to BBDI-resistant SUM149R or SUM159R cells (Figure S1E), none of the mutated genes overlapped with CRISPR screen hits, suggesting that they may not play a role in BBDI response and resistance. BBDI-resistant cell lines displayed a significant increase in global DNA methylation that was not affected by JQ1 (Figure S1F). Although this increase in DNA methylation did not globally correlate with changes in gene expression, a number of genes (e.g., *DBC1* and *PTN*) showed significant changes in both DNA methylation and expression (Figure S1G). Histone mass spectrometry revealed increased H3K27me2, H3K27me3, H3K9me0, H3K9me1, H3K9me2, and H3K9me3 levels in both BBDI-resistant cell lines compared with parental cells, but JQ1 treatment did not influence these profiles (Figure S1H).

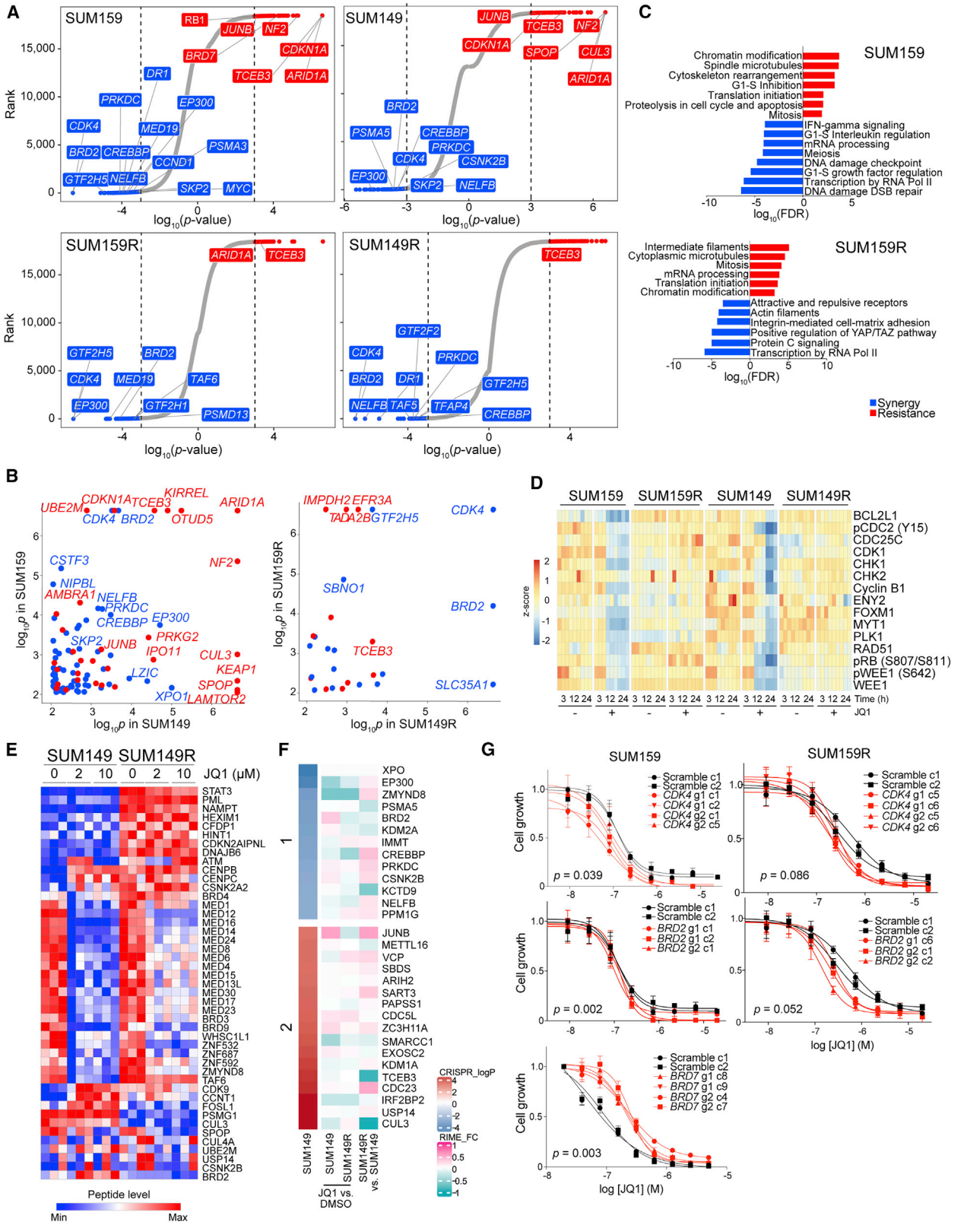

(legend on next page)

Functional analysis of differentially expressed genes by Metacore (Nikolsky et al., 2005) revealed upregulation of G1-S growth factor regulation, anti-apoptosis, and epithelial-to-mesenchymal transition (EMT) pathways in resistant compared with parental cells, whereas G2-M, mitosis, and ubiquitin-proteasomal proteolysis were downregulated (Figure S1I; Table S2). Cell cycle-related pathways were downregulated by JQ1 in parental but upregulated in BBDI-resistant cells. Reverse-phase protein array (RPPA) (Tibes et al., 2006) analysis revealed 12 clusters that showed differences because of JQ1 treatment or BBDI resistance (Figure S2A; Table S3), with altered proteins enriched in several oncogenic pathways, including NOTCH, WNT, and JAK-STAT signaling (Figure S2B). Specifically, c-MYC, epidermal growth factor receptor (EGFR), and phospho-EGFR, JAK2, and $STAT3^{pT705}$ were elevated in SUM149R cells; YAP had increased expression and phosphorylation (S127) in SUM159R cells; and BCL2, cyclin D1, AXL, BRD4, HER2, STAT5A, and c-MET had higher levels in both BBDI-resistant lines (Figure S2C). Cluster 8, composed of cell cycle-related proteins, was downregulated by JQ1 in parental but not in BBDI-resistant cells (Figure 1D). The average expression of all cell cycle proteins based on RPPA showed a similar trend (Figure S2D), indicating that JQ1 has the most pronounced effects on the cell cycle compared with other cellular programs. These gene expression and protein changes are consistent with our CRISPR screen data showing that deletion of positive regulators of G1-S progression (e.g., *CCND1* and *CDK4*) sensitizes cells to JQ1, whereas deletion of negative regulators (e.g., *RB1* and *CDKN1A*) increases JQ1 resistance. The expression levels of several CRISPR screen hits were also differentially regulated in parental and resistant cells with or without JQ1 treatment, including *CDK4* and *BRD2* (Figures S2A–S2F). Similarly, the YAP-TAZ pathway, which is specifically upregulated in SUM159R cells, based on RNA sequencing (RNA-seq) and RPPA data, was essential only in SUM159R cells (Tables S1, S2, and S3). These results suggest that JQ1 has the most pronounced effects on signaling pathways and cell cycle proteins regulating G1-S transition.

To characterize BRD4-associated chromatin complexes, we performed rapid immunoprecipitation mass spectrometry of endogenous proteins (RIME) and quantitative multiplexed RIME (qPLEX-RIME) (Mohammed et al., 2013; Papachristou et al., 2018) in parental and BBDI-resistant cells in the presence and absence of JQ1. We found that JQ1 disrupted BRD4's interaction with Mediator proteins and epigenetic regulators in both parental cells, whereas there was less change in BBDI-resistant cells (Figures 1E and S2G; Table S3). Many of the BRD4-interacting proteins we identified are also part of the BRD4 interactome in other cell types, implying a general role in BRD4 function (Lambert et al., 2019). CK2 and STAT3 showed increased binding with BRD4 in SUM149R cells (Figure 1E), which we confirmed for STAT3 by co-immunoprecipitation (Figure S2H). On the other hand, enzymes involved in ubiquitination (CUL3 and SPOP) showed the opposite trend (Figure 1E). Analysis of process networks enriched in differentially bound proteins identified the RNA polymerase II (RNA Pol II) complex as most significantly decreased by JQ1 in parental cells, whereas mRNA processing was the most significantly increased pathway in resistant cells after JQ1 (Figure S2I). The RNA Pol II pathway and chromatin modification complex were the top upregulated process networks in SUM149R compared with SUM149 cells, whereas cytoskeleton rearrangement and mitosis were the top downregulated ones (Figure S2I). Several BRD4-associated proteins were top CRISPR screen hits, including the bromodomain proteins BRD2, ZMYND8, EP300, as well as BRD4 modifiers such as CSNK2B and CUL3 (Figures 1F and S2J).

In summary, our multi-omics profiling of differences between BBDI-sensitive and -resistant cells before and after JQ1 provide a strong mechanistic explanation for many of the hits we identified in our CRISPR screen.

Validation of CRISPR Screen Hits

In our CRISPR screen, positive and negative regulators of G1-S progression were among the top synergistic and resistance hits, respectively, and RNA-seq and RPPA analyses demonstrated that JQ1 has the most pronounced effects on the cell cycle. Because our ultimate goal is to test BBDI combination therapies in the clinic, and CDK4/6 inhibitors are already approved for treatment of ER^+ breast cancer (Abraham et al., 2018), we selected CDK4 for further validation. Similarly, we decided to further characterize BRD2 and BRD7 because they were top CRISPR synergy and resistance hits, respectively, and are implicated in JQ1 response based on gene expression and proteomics changes. The read counts of multiple sgRNAs targeting *CDK4* and *BRD2* displayed specific depletion after JQ1 in SUM159R and SUM149R cells, whereas *BRD7* sgRNAs showed uniform positive selection in SUM159 cells (Figure S3A).

To further validate the relationships between JQ1 treatment and *CDK4*, *BRD2*, and *BRD7*, we generated single-cell clones of SUM159 and SUM159R cells expressing individual sgRNAs targeting *CDK4* and *BRD2* as well as SUM159 clones expressing *BRD7* sgRNAs (Figure S3B). SUM159 and SUM159R single-cell

Figure 1. CRISPR Screen Results and Molecular Profiles

(A) Top hit genes in the CRISPR screen revealed by comparing untreated with JQ1-treated cells. Genes are ranked by $\log_{10}$(p values) defined by MAGeCK. Significant resistance and synthetic lethal hits ($p < 0.001$) are marked in red and blue, respectively.

(B) Comparison of CRISPR screen hits between the indicted cell lines. Genes with $p < 0.001$ defined by MAGeCK in both cell lines are shown.

(C) Top process networks enriched in CRISPR screen hits.

(D) Heatmap of cluster 8 in RPPA data representing proteins downregulated after JQ1 treatment in parental but not in BBDI-resistant cells.

(E) Heatmap of BRD4 RIME data in SUM149 and SUM149R cells with or without 3-h JQ1 treatment at the indicated doses.

(F) Heatmap of significant resistant (red) and synthetic lethal (blue) CRISPR screen hits and their BRD4 binding changes, revealed by RIME in SUM149 and SUM149R cells in JQ1 compared with DMSO and in SUM149R compared with SUM149 cells.

(G) Dose-response curves of JQ1 of scramble or gene-specific sgRNA-expressing single-cell clones derived from the indicated cell lines. The p values indicate the statistical significance of differences compared with scramble sgRNA based on unpaired t tests. Data are represented as mean ± SEM.

See also Figures S1–S3 and Tables S1, S2, and S3.

clones with *BRD2* or *CDK4* deletion displayed increased sensitivity to JQ1 compared with scrambled sgRNA-expressing clones (Figures 1G and S3C). In contrast, SUM159-derived *BRD7* knockout clones were more resistant to JQ1 than clones expressing scrambled controls (Figures 1G and S3C). Overexpression of doxycycline-inducible CDK4 rescued the decreased viability of *CDK4* knockout clones after JQ1 treatment, validating it as an on-target effect (Figures S3D and S3E).

Small-Molecule Inhibitor (SMI) Screen

To identify therapeutic compounds to overcome BBDI resistance, we performed a cellular viability screen in parental and resistant cells, using two SMI libraries targeting a range of pathways (Figure S3F; Table S4). We confirmed the resistance of SUM159R and SUM149R cells to JQ1 and to other BBDIs (Figures 2A–2D and S3G). To identify potentially synergistic compounds, we identified drugs to which the BBDI-resistant lines were more sensitive than the parental lines (Figure S3H). In SUM149R cells, top hits included DNA damage-inducing agents (topoisomerase, DNA synthesis, and microtubule), cell cycle (CDK4/6, PLK, and AURK), histone deacetylase (HDAC), and HSP90 inhibitors (Figures 2A and 2B). Several cell cycle inhibitors targeting CDK4/6, AURK, and PLK especially effectively inhibited growth of SUM149R compared with SUM149 cells (Figure 2A). For several selected hits, we confirmed synergy with JQ1 in SUM149R cells (Figure S3I) and inhibition of their target (Figure S3J). Signaling pathways were most frequent among the top hits in SUM159R cells, including EGFR, MEK, and phosphatidylinositol 3-kinase (PI3K), as well as transforming growth factor β (TGF-β) and endocrine inhibitors (Figures 2C and 2D), which is consistent with our RPPA and RNA-seq data demonstrating upregulation of these pathways in resistant cells (Figures S1I and S2A–S2F). BCL2 inhibitors were hits in SUM149R and SUM159R cells (Figures 2A and 2C), consistent with our previous findings that upregulation of anti-apoptotic factors contributes to JQ1 resistance (Shu et al., 2016). Topoisomerase inhibitors were hits for SUM159R and SUM149R cells (Figures 2A and 2C), which may reflect sensitivity to DNA damage and transcription, which we also found in our CRISPR screen (Figures 1C and S1D). Furthermore, both BBDI-resistant lines had increased sensitivity to inhibitors of CDK9, a component of the P-TEFb complex with BBD proteins, as well as the non-specific CDK inhibitor AT7519, and SUM149R cells were also more sensitive to the CDK4/6-specific inhibitor palbociclib (Figures 2E and 2F). These findings are in line with our CRISPR and molecular profiling data indicating that G1-S cell cycle progression and transcriptional activators become more essential in cells with acquired BBDI resistance. The identification of the same genes and pathways using multiple independent unbiased methods and the integration of these findings with molecular profiles highlight the robustness of the data and the advantage of using such a combined approach.

Combination Treatments *In Vitro* and *In Vivo*

To further validate synthetic lethal targets identified in our CRISPR knockout and SMI screens, we performed synergy screens in SUM149, SUM149R, SUM159, and SUM159R cells. We prioritized US Food and Drug Administration (FDA)-approved drugs to facilitate clinical translatability of our results. We found that, in general, most of these drugs were more synergistic in the resistant compared with the parental lines, in which they were additive or antagonistic. Several DNA-damaging agents (e.g., doxorubicin) and microtubule inhibitors (e.g., vincristine) showed significant synergy with JQ1 in SUM149R cells, whereas the kinase inhibitor dasatinib and the YAP-TAZ inhibitor verteporfin were synergistic in SUM159R cells (Figure 3A; Table S4). Paclitaxel, a microtubule inhibitor, and TP0903, an AXL kinase inhibitor, were synergistic in both BBDI-resistant lines (Figure 3A). Notably, palbociclib had the most significant synergy in all parental and resistant cell lines as well as in several other TNBC cell lines, and this was independent of *RB1* mutation status (Figures 3A and S4A).

To validate these *in vitro* synergy results *in vivo*, we tested the sensitivity of SUM149R and SUM159R and a patient-derived xenograft (PDX; IDC50) to selected combinations. JAK2 (INC424) and BCL2 and BCL-XL (ABT-263 and ABT-199) inhibitors significantly decreased tumor weight even as single agents in SUM159R xenografts, whereas combination of all of these agents with JQ1 resulted in significantly smaller tumors in SUM149R and SUM159R xenografts (Figure 3B). The partial JQ1 responsiveness of JQ1-treated SUM159R xenograft reflects the heterogeneity of this cell line. Hematoxylin and eosin (H&E)-stained slides and caspase-3 immunofluorescence demonstrated an increase in apoptosis in combination treatments (Figures 3C, S4B, and S4C). We also detected a more significant decrease in phospho-STAT3 positivity with JQ1+INC424 treatment (Figure S4D). Similarly, palbociclib and JQ1 combination significantly decreased the growth and final tumor weight of SUM159R and IDC50 xenografts with a concomitant decrease in phospho-RB positive cells (Figures 3D and S4E–S4G). In the IDC50 PDX, we even observed slight regression with the combination despite the short treatment because of the extremely fast growth of this tumor.

To explore the mechanism of synergy between palbociclib and JQ1, we analyzed the protein levels and activity of key regulators of G1-S progression as well as BRD2, BRD4, and BRD7 by immunoblots in SUM149R and SUM159R cells. JQ1 treatment increased BRD2 and CCND1 and RB phosphorylation, whereas palbociclib decreased BRD2, BRD4, E2F1, and RB phosphorylation in a dose- and time-dependent manner, more markedly in SUM159R than in SUM159 and SUM149R cells (Figures 3E and S4H). These findings suggest that palbociclib can enhance sensitivity to JQ1 via multiple mechanisms, including CDK4 inhibition-mediated G1 arrest, as well as by enhancing proteasomal degradation of BRD2 and BRD4, potentially through CDK4-regulated ubiquitination in an RB-independent manner (Jin et al., 2018).

Targeted BET Protein Degradation Overcomes BBDI Resistance

Because BBDI-resistant cells are still dependent on BRD2 and BRD4 (Shu et al., 2016) and modulating BBD protein levels is one of the most effective ways to modulate JQ1 sensitivity, based on our CRISPR screen and multi-omics data, we tested whether targeted degradation of BBD proteins would overcome BBDI resistance. We recently developed a highly potent and

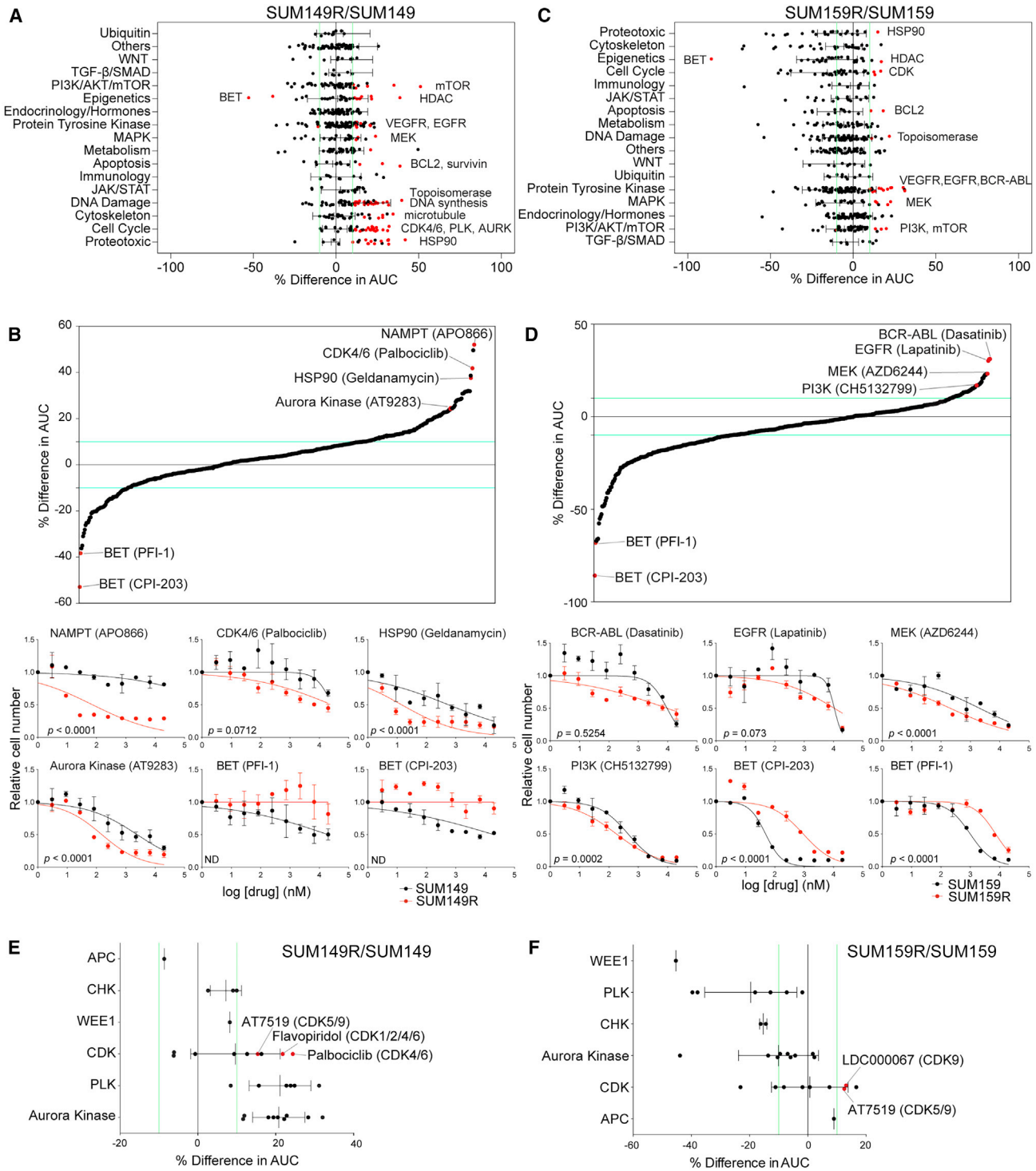

Figure 2. Small-Molecule Screen in BBI-Resistant TNBC Cells

(A–D) Differences in drug sensitivities between SUM149R and SUM149 (A and B) and between SUM159R and SUM159 cells (C and D), grouped by pathways targeted by drugs in the library (A and C) and ordered by percent differences in area under the curve (AUC) (B and D). Common targets of top hits are indicated (A and C), and individual dose-response curves of top hits are shown (B and D). The p values indicate the statistical significance of differences. Data are represented as mean ± SD.

(E and F) Differences in sensitivities of drugs targeting the cell cycle, grouped by target, in SUM149R/SUM149 (E) and SUM159R/SUM159 cells (F).

See also Figure S3 and Table S4.

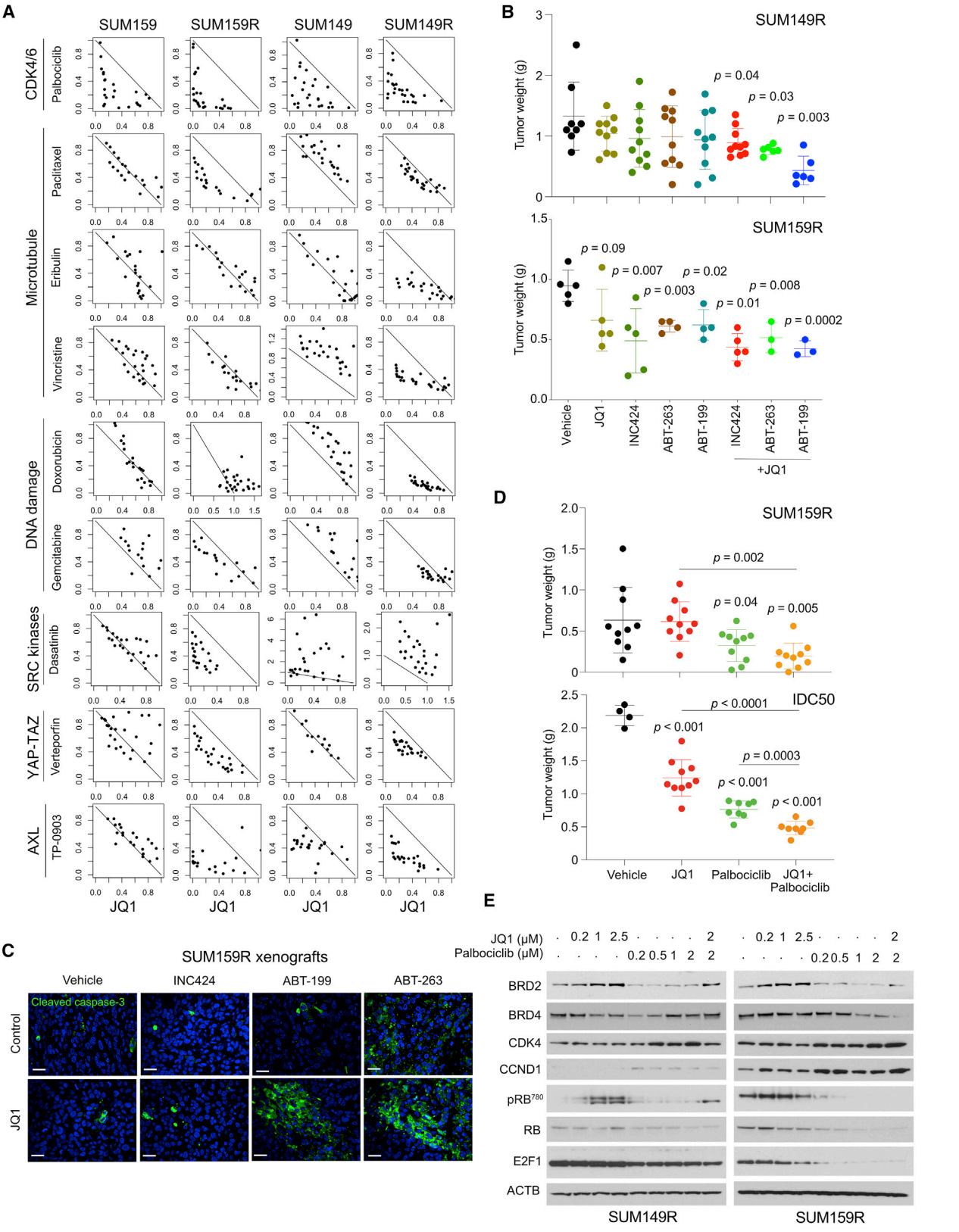

(legend on next page)

selective small-molecule degrader, dBET6, with improved cellular permeability and improved efficacy (Winter et al., 2015, 2017). dBET6 is a bifunctional molecule consisting of JQ1 appended to phthalimide conjugates via a longer linker compared with dBET1 (Figure S4I). We first tested the effect of these BBD degraders on cellular viability in a panel of TNBC lines and confirmed the highest efficacy of dBET6 (Figure 4A). Both the SUM149R and SUM159R lines were significantly more sensitive to dBET6 compared with JQ1 (Figure 4B). dBET6 potently degraded BRD2, BRD3, and BRD4 in a dose-dependent manner in parental and BBDI-resistant cells (Figures 4C and S4J). Consistent with degradation of BRD4 protein, we observed global loss of BRD4 from chromatin in SUM149R cells (Figures 4D and 4E), accompanied by a decrease in mRNA levels across the majority of active genes (Figures 4F and S4K) and a decrease in RNA Pol II phosphorylation (Figure S4J). Thus, dBET6 treatment results in rapid degradation of BRD4-bound chromatin, which, in turn, causes a global reduction in active gene transcription mediated in part by loss of initiating and elongated RNA Pol II.

To further investigate dBET6 efficacy *in vivo*, we treated SUM149R and SUM159R xenografts with JQ1 or dBET6. Although dBET6 more efficiently decreased tumor weight compared with JQ1, with a concomitant decrease in BRD4 protein levels (Figures 4G, S4L, and S4M), we had to discontinue the experiment after 10 days of treatment because significant toxicity. A lower dose (7.5 mg/kg) of dBET6 still significantly decreased tumor weight in SUM149R xenografts (Figure 4H). These data show that BBD protein degradation overcomes BBDI resistance in the SUM149R and SUM159R cell lines in cell culture and *in vivo*.

The Effect of Functional Differences between Bromodomain Proteins on BBDI Response and Resistance

To investigate whether identification of *BRD2* and *BRD7* as top synthetic lethal and resistance hits, respectively, in our CRISPR screen is due to differences in chromatin binding and the sensitivity of this to JQ1, we performed chromatin immunoprecipitation sequencing (ChIP-seq) for BRD2, BRD4, BRD7, and H3K27ac (histone H3 lysine 27 acetyl) as well as assay for transposase-accessible chromatin using sequencing (ATAC-seq) in the presence and absence of JQ1. We found that BRD4, BRD2, and H3K27ac bind to the same promoters and enhancers in SUM159 and SUM149 cells (Figures 5A and S5A). Although BRD4 and BRD2 binding was decreased after JQ1 treatment (Figures 5B and S5B), and this was highly correlated in promoter and enhancer regions (Figures 5C and S5C), the decrease was more significant for BRD4 than BRD2. This finding indicates that BRD2 is less efficiently dissociated from chromatin by JQ1 than BRD4, potentially explaining why BRD2 was a top synergy hit in our CRISPR screen whereas BRD4 was not. We observed an increase of BRD4 and BRD2 binding in the same promoter and enhancer regions in SUM159R cells compared with parental cells (Figures 5B, 5C, S7B, and S7C). Recent reports described that, in hematopoietic cells, BRD2, but not BRD4, colocalizes with CTCF and enhances its insulator function (Cheung et al., 2017; Hsu et al., 2017). However, in TNBC cells, we found that CTCF binding was correlated with all proteins analyzed (BRD2, BRD4, and BRD7) (Figure S5D). We then investigated the effects of these binding changes on transcription and found that alterations in BRD4 binding were associated with gene expression changes, especially at SE loci (Figures 5D and S5E), including SEs near *BRD2* and *CCND1* (Figures 5E and S5F).

BRD7 binding was detected at the same regions as BRD4 and BRD2; however, BRD7 binding increased after JQ1 treatment at the same loci where the BRD4 and BRD2 signal decreased in SUM159 cells, whereas it decreased in SUM159R cells (Figures 5B and 5C). This anti-correlation between - BRD2, BRD4, and BRD7 chromatin binding after JQ1 treatment explains our CRISPR screen data, which identified BRD2 and BRD7 as synthetic lethal and resistance hits, respectively, in SUM159 cells.

To investigate the effect of *BRD7* deletion on the chromatin landscape and gene expression patterns, we performed ATAC-seq and RNA-seq, respectively, in *BRD7* knockout (KO) cells. Intriguingly, the transcriptomic profile of *BRD7* KO cells was highly similar to that of SUM159R cells at the gene and pathway levels and under DMSO and JQ1 treatment conditions (Figures 5F, 5G, S5G, and S5H; Table S5). Top enriched process networks included NOTCH, ESR1, and Hh signaling. We also calculated luminal-basal-mesenchymal signature scores of wild-type (WT) and *BRD7* KO cells because our prior data indicated that BBDI resistance is associated with gain of luminal features (Shu et al., 2016). *BRD7* KO cells had increased luminal and decreased mesenchymal scores (Figure S7I), suggesting that deleting BRD7 may shift the cells to a more luminal phenotype associated with BBDI resistance.

ATAC-seq demonstrated gain and loss in promoter regions in *BRD7* KO cells compared with the WT (Figure 5H), and these alterations in open chromatin were correlated with gene expression changes (Figures 5I and S5J). Comparison of ATAC-seq profiles of *BRD7* KO and WT clones as well as parental

Figure 3. Validation of Synthetic Lethal Interactions with JQ1

(A) Synergy studies of JQ1 with various inhibitors in cell culture. Points represent paired values of drug concentrations assessed for synergism (STAR Methods). The diagonal line signifies drug additivity. Points above and below the line represent antagonistic and synergistic drug combinations, respectively.

(B) Plots show xenograft weights after treatment with JQ1 (50 mg/kg daily) and other drugs alone and in combination. The p values indicate the statistical significance of differences compared with vehicle based on unpaired t test. Data are represented as mean ± SD.

(C) Immunofluorescence analysis of cleaved caspase-3 in SUM159R xenografts after single and combination treatments. Scale bars represent 50 μm.

(D) Plots show xenograft weights after treatment with JQ1 (30 mg/kg daily) and palbociclib, alone and in combination. The p values indicate the statistical significance of differences compared with vehicle based on unpaired t test. Data are represented as mean ± SD.

(E) Immunoblot analysis of the indicated proteins in SUM149R and SUM159R cells treated with the indicated doses of JQ1, palbociclib, and their combination for 12 h.

See also Figure S4.

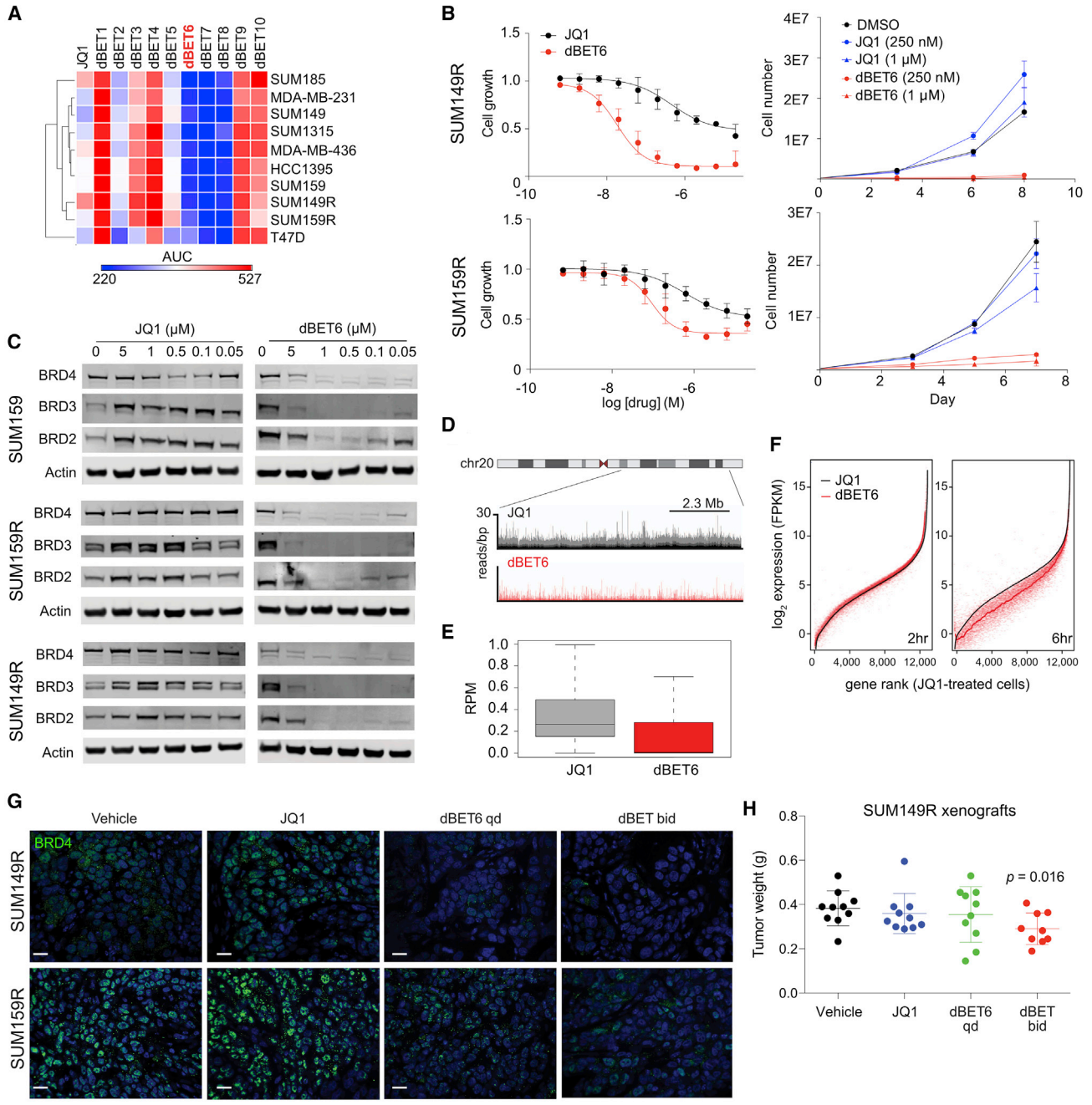

Figure 4. Targeted BET Degradation in TNBC

(A) Heatmap of sensitivities to JQ1 and dBET series by surrogate levels of ATP content. Results of 10-point dose response curves after 72 h of treatment are represented by AUC.

(B) Dose-response curves (left) and growth curves (right) of JQ1 and dBET6 at the indicated concentrations in SUM149R and SUM159R cells. The p values indicate the statistical significance of differences compared with DMSO. Data are represented as mean ± SD.

(C) Immunoblot analysis of BRD2, BRD3, and BRD4 levels after 4 h of treatment with JQ1 and dBET6 in SUM159, SUM159R, and SUM149R cells.

(D) ChIP-seq tracks of BRD4 levels on chromosome 20 in SUM149R cells. The top track (black) shows the basal resistance state in the presence of 10 μM JQ1, and the bottom track (red) shows 2 h of treatment with 250 nM dBET6.

(E) Boxplot of the global levels of chromatin-bound BRD4 after treatment with 10 μM of JQ1 and 250 nM dBET6 for 2 h. RPM, reads per million.

(F) Expression levels of all active genes ranked by their expression after treatment with JQ1 for 2 h (left) and dBET6 for 6 h (right).

(G) Immunofluorescence analysis of BRD4 in SUM149R and SUM159R xenografts treated with JQ1 (50 mg/kg daily) or dBET6 (7.5 mg/kg once - qd or twice daily - bid). Scale bars represent 50 μm.

(H) Tumor weights of SUM149R xenografts following 2 weeks of treatment with JQ1 or dBET6. The p value indicates the statistical significance of difference compared with vehicle based on a unpaired t test. Data are represented as mean ± SD.

See also Figure S4.

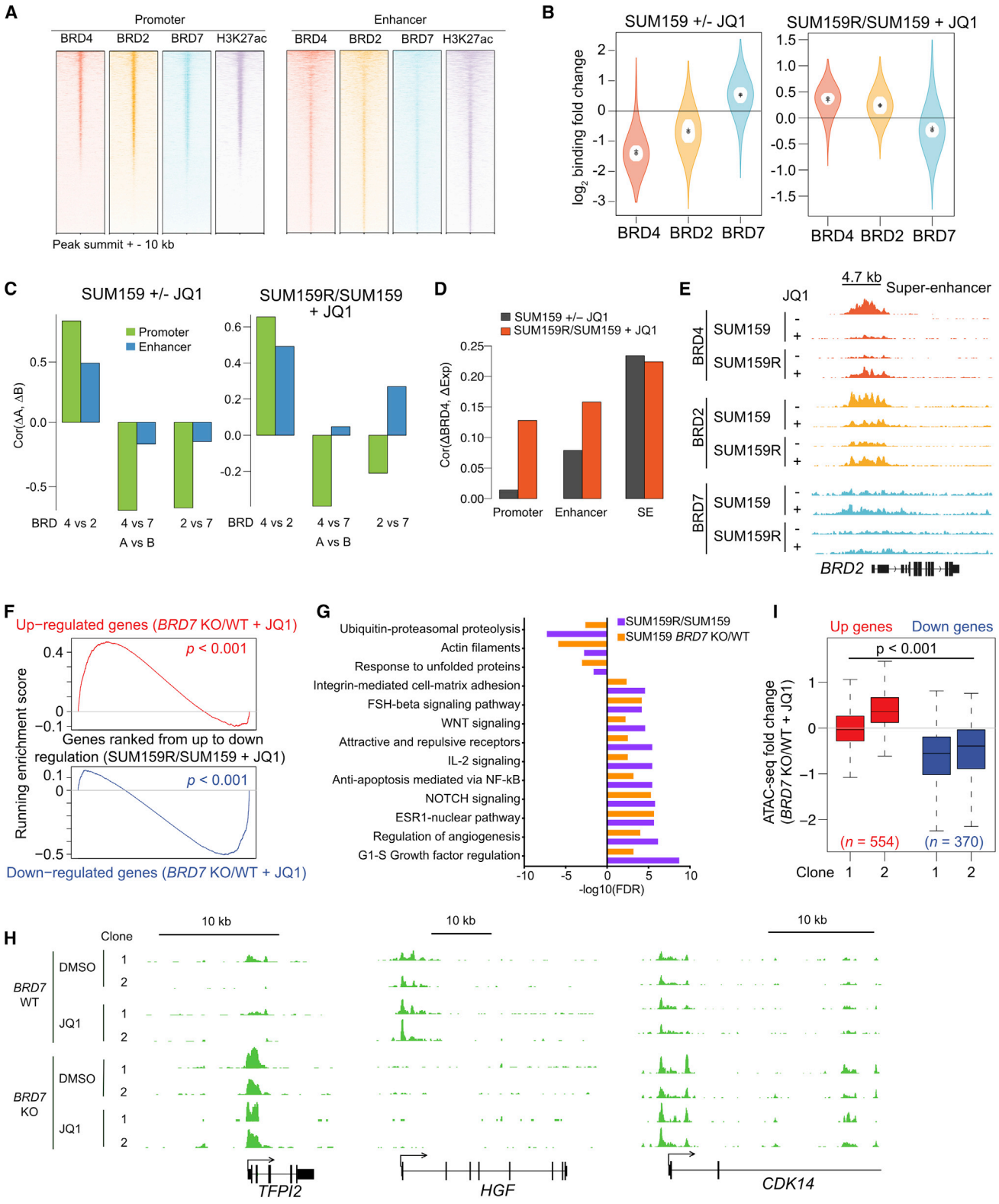

(legend on next page)

SUM159 and BBDI-resistant SUM159R cells demonstrated higher relatedness of *BRD7* KO clones to SUM159R cells, whereas parental SUM159 cells clustered with scrambled controls (Figure S5K). These results indicate that deletion of *BRD7* changed the chromatin landscape of SUM159 cells, making them more similar to BBDI-resistant SUM159R cells. Analysis of ATAC-seq peaks gained in *BRD7* KO cells and associated with increased gene expression revealed significant overlap with YAP1 peaks in the CISTROME database and enrichment in the TEAD motif, suggesting upregulation of YAP1-TEAD transcriptional activity (Figure S5L). Interestingly, our RNA-seq and RPPA analyses as well as our CRISPR screen also identified the YAP-TAZ pathway as upregulated and essential in SUM159R cells, highlighting a role of this pathway in BBDI resistance.

The Effect of BRD7 Loss on BRD4 Chromatin Binding and Histone Modification Patterns

To further investigate the role of BRD7 in BRD4 chromatin binding and histone modification patterns, we performed ChIP-seq for BRD4, H3K27ac, H3K4me3, and H3K27me3 in SUM159 *BRD7* WT and KO cells. Combined analysis of the multi-omics data revealed a positive correlation between changes in BRD4 binding and changes in ATAC-seq, RNA-seq, H3K4me3, and H3K27ac following BRD7 deletion at SEs and, less pronouncedly, at promoters (Figure S6A). Assessing changes in BRD4 binding at genomic loci also bound by BRD7 in WT cells showed that changes in BRD4 binding were associated with changes in the same direction in H3K27ac, H3K4me3, ATAC-seq signal, and mRNA levels (Figure S6B).

To gauge changes in the SE landscape in BRD7 KO cells and the similarities of this to JQ1-resistant SUM159R cells, we analyzed differences in H3K27ac signal in SEs between BRD7 WT and KO and SUM159 and SUM159R cells. Interestingly, many of the SEs gained in SUM159R cells were also gained in BRD7 KO cells, including *BCL2L1* (Figures 6A and 6B). We further analyzed the changes in H3K27ac signal in BRD7 KO cells in relation to BRD4 genomic binding at SEs and promoters. In both regions, the most significant H3K27ac increase in BRD7 KO cells occurred at loci bound by BRD4 in a JQ1-dependent manner in SUM159 and SUM159R cells (Figures 6C and S6C). These changes in H3K27ac were also correlated with changes in ATAC-seq signal and expression of the associated genes. Specifically, the top 1,000 JQ1-sensitive BRD4 binding sites and the top 1,000 downregulated genes by JQ1 showed the most pronounced changes in H3K27ac, H3K4me3, and ATAC-seq signal in BRD7 KO compared with BRD7 WT cells (Figures 6D and 6E); we found that the former demonstrated significantly larger changes in these markers compared with the latter, suggesting that changes in chromatin modifications are more pronounced than gene expression changes. These data indicate that loss of BRD7 does not significantly affect BRD4 chromatin binding but increases H3K27ac and H3K4me3 signals in BRD4-dissociated regions by JQ1 and increases the expression of genes downregulated by JQ1 in SUM159 cells. Thus, these alterations in H3K27ac and gene expression profiles make BRD7 KO cells resistant to JQ1.

Clinical Significance of BRD4 and BRD7 Expression in TNBC

To investigate the clinical relevance of BRD4 and BRD7 interaction in breast cancer, we analyzed their expression patterns in the TCGA cohort (Cancer Genome Atlas Network, 2012). *BRD4* and *BRD7* have significantly higher expression in basal compared with luminal breast tumors, which is in contrast to *ARID1A*, a subunit of the BAF complex implicated in luminal differentiation (Nagarajan et al., 2020; Xu et al., 2020; Figure S6D). Even within TNBC, the highest BRD4 and BRD7 expression was observed within basal subtype tumors (Figure S6E), implying that BRD4 and BRD7 function may be particularly relevant in non-luminal breast tumors. Further analysis demonstrated that TNBC patients with lower expression of BRD4 or BRD7 had shorter disease-free survival, and this was especially the case when both genes had low expression levels (Figure S6F). BRD7 expression levels were also associated with expression of the JQ1 resistance gene signature derived from our cell line data; low-BRD7-expressing tumors have a high JQ1 resistance score (Figure S6G), validating the relevance of our data in human breast tumor samples.

Single-Cell Profiling of BBDI-Resistant Cells

We recently described that higher cellular transcriptomic heterogeneity is associated with therapeutic resistance and that

Figure 5. BRD4, BRD2, and BRD7 Binding Changes and Their Effects on JQ1 Treatment

(A) ChIP-seq binding enrichment of BRD4, BRD2, BRD7, and H3K27ac in promoter and enhancer regions in SUM159 cells.

(B) BRD4, BRD2, and BRD7 ChIP-seq binding changes between JQ1-treated (+JQ1) and untreated (−JQ1) SUM159 cells and between JQ1-treated resistant (SUM159R) and parental cells. The outer violin indicates the entire distribution, the inner violin (white) indicates the interquartile range, and ''.'' and ''+'' indicate the median and mean, respectively.

(C) Pairwise correlations of BRD4, BRD2, and BRD7 ChIP-seq binding changes in promoter and enhancer regions.

(D) Correlations of BRD4 binding changes in promoter, enhancer, and SE regions and their gene expression changes.

(E) Gene tracks depicting BRD4, BRD2, and BRD7 signals at the *BRD2* locus.

(F) Gene set enrichment analysis (GSEA) depicting the relationship between expression of genes in JQ1-treated *BRD7* KO cells and JQ1-treated resistant cells. p-value was obtained from GSEA.

(G) Top process networks enriched in differentially expressed genes between JQ1-treated BRD7 wild-type (WT) and *BRD7* knockout (KO) SUM159 cells and between JQ1-treated SUM159R and SUM159 cells.

(H) Gene tracks depicting ATAC-seq signals at selected genomic loci in SUM159 *BRD7* WT and KO cells.

(I) Association between ATAC-seq binding changes and gene expression changes in two JQ1-treated *BRD7* KO clones compared with JQ1-treated WT SUM159 cells. Wilcoxon rank-sum test p value is shown.

See also Figure S5 and Table S5.

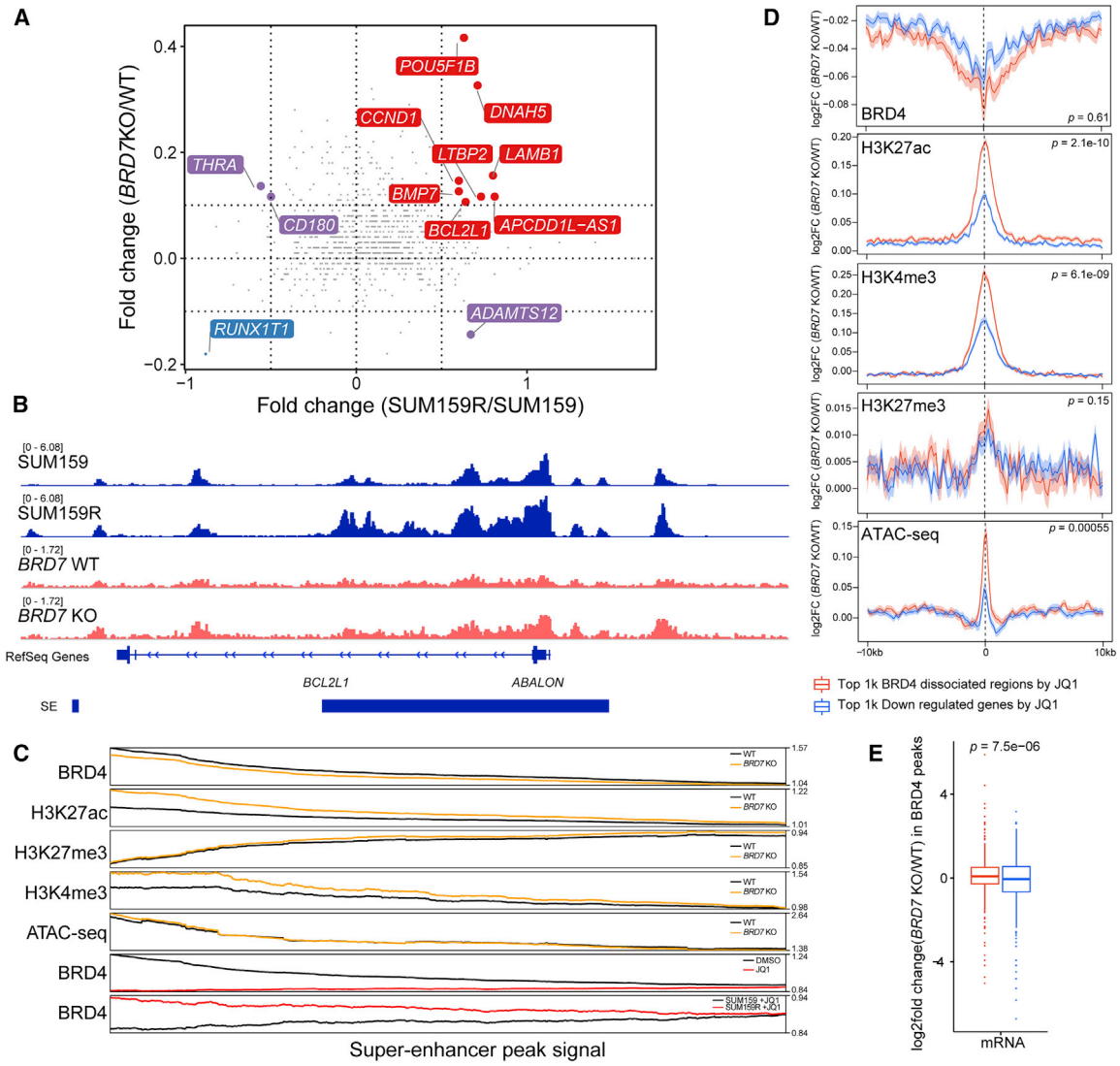

Figure 6. The Effects of BRD7 Deletion on BRD4 Binding and Histone Modification Patterns

(A) Changes in SEs upon BRD7 KO and between JQ1-sensitive and -resistant SUM159 cells. Red indicates co-activated super-enhancers; blue represents co-repressed super-enhancers. Purple indicates discrepant regulated super-enhancers.

(B) Example of a differential H3K27ac signal in a SE region. Normalized H3K27ac ChIP-seq signals (reads per million) are shown as tracks using Integrative Genomics Viewer.

(C) Line plot showing smoothed signals of BRD4, H3K27ac, H3K27me3, and H3K4me3 ChIP-seq and ATAC-seq in BRD7 KO and scramble SUM159 cells at SEs and comparison with BRD4 ChIP-seq signals in DMSO-treated, JQ1-treated, and JQ1-resistant SUM159 cells (bottom two tracks). SEs are ranked by the fold change of BRD4 signal between ± JQ1 from high (left) to low (right).

(D) Changes in BRD4, H3K27ac, H3K27me3, H3K4me3, and ATAC-seq signals at the top 1,000 BRD4 binding sites sensitive to JQ1 in SUM159 cells (red) and at the top 1,000 genes downregulated by JQ1 in SUM159 cells (blue). ChIP-seq signals on peak summit ± 10-kb region. Wilcoxon rank-sum test p values are shown.

(E) Changes in mRNA levels at BRD4 peaks differential between BRD7 KO and WT cells at the top 1,000 BRD4 binding sites sensitive to JQ1 in SUM159 cells (red) and at the top 1,000 genes downregulated by JQ1 in SUM159 cells (blue). Wilcoxon rank-sum test p value is shown.

See also Figures S6.

epigenetic regulators modulate this heterogeneity (Hinohara et al., 2018). To assess whether cellular transcriptomic heterogeneity also plays a role in BBDI resistance and whether it is modulated by JQ1, we performed single-cell RNA-seq (scRNA-seq) profiling of parental and BBDI-resistant cells before and after JQ1 treatment. Untreated and JQ1-treated cells formed distinct clusters in all four lines tested, indicating that JQ1 significantly alters cellular transcriptomes (Figures 7A and S7A). Similarly, BBDI-resistant and parental cells separated very clearly, and BBDI-resistant cell cluster-specific genes included several CRISPR screen hits, such as *CDK4*, *CCND1*, and *BCL2L1* (Figures 7A and S7A). Although both parental cell lines and SUM149R cells formed a single cell cluster, SUM159R cells split into two groups under untreated and JQ1-treated conditions

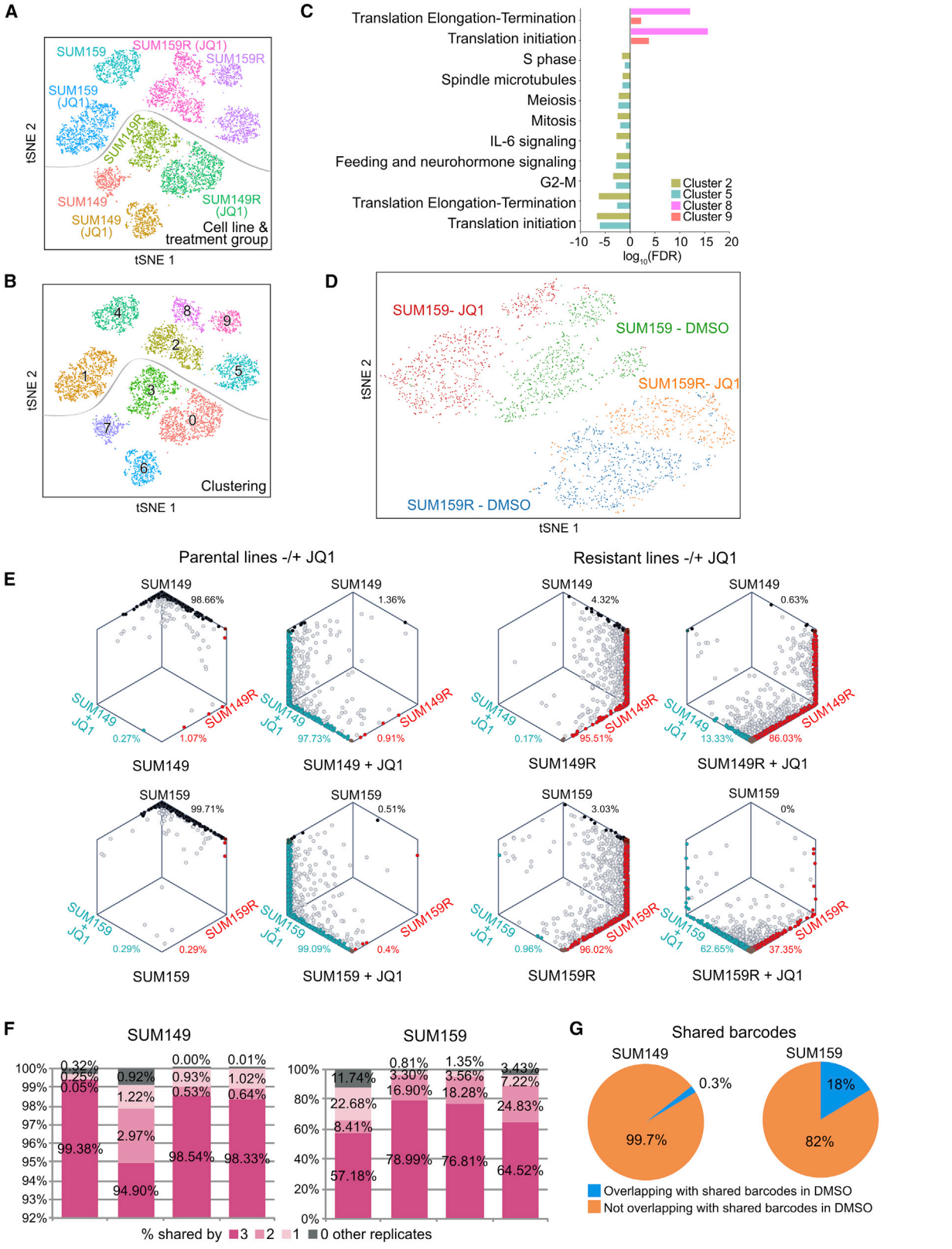

(legend on next page)

(Figure 7B). These two subgroups did not appear to be proliferation-related, based on the expression of cell-cycle-related genes (Figure S7B), but cluster-specific genes showed enrichment in translation-related functional categories (Figure 7C). Because our prior data indicated that luminal breast cancer cells in general are less sensitive to BBDIs than basal and mesenchymal ones (Shu et al., 2016), we also quantified basal, luminal, and mesenchymal signature scores for each single cell. We observed that SUM159R cells had higher luminal scores compared with SUM159 cells and that this pattern was further increased by JQ1 (Figure S7C), confirming that gain of luminal features is associated with BBDI resistance. The SUM159R subclusters did not show significant differences in luminal-basal signature scores besides the lower mesenchymal and higher luminal scores observed after JQ1 treatment (Figure S7C). However, analysis of the chromosomal location of cluster-defining genes demonstrated that ~30% of genes specific for clusters 8 and 9 are localized to chromosome 11 (many on 11q), in contrast to 10%–17% in clusters 2 and 5 (Table S6), suggesting that cells in clusters 8 and 9 may have gain of this chromosomal region. *CCND1* and *YAP1* are located on chromosome 11q, and they are cluster 8 and 9 marker genes, highlighting their role in BBDI resistance.

We also performed single-cell ATAC-seq (scATAC-seq) to assess potential cellular epigenetic heterogeneity, which could underlie clustering of the cells, based on scRNA-seq. Pooled scATAC-seq correlated very well with ATAC-seq on bulk cell populations, confirming the quality of the data (Figure S7D). Interestingly, the cell lines clustered differently based on scATAC-seq compared with scRNA-seq. Control and JQ1-treated SUM159R cells formed one large cluster without clear separation of the two treatment conditions (Figure 7D). In contrast, JQ1-treated SUM159 cells were clearly distinct from DMSO-treated controls. These data demonstrate that SUM159R cells are epigenetically distinct from SUM159 cells and that their epigenetic state is less responsive to JQ1 treatment than that of SUM159 cells.

To further investigate differences in BBDI resistance mechanisms between the two cell lines and the heterogeneity of SUM159R cells, we explored our scRNA-seq data to determine whether we could detect rare cells with gene expression signatures of BBDI-resistant cells prior to treatment and whether the gene expression profiles of BBDI-resistant and BBDI-treated cells are related. Thus, we selected genes differentially expressed between parental and BBDI-resistant or JQ1-treated parental cells based on bulk RNA-seq data (Figure S1I; Table S2) and investigated whether single cells could be classified into one of these three transcriptionally distinct groups (i.e., parental, resistant, and JQ1-treated). Although most single cells in SUM149R and SUM159R populations were classified as resistant, very few such cells were present in parental and in JQ1-treated populations (Figure 7E), suggesting that JQ1-resistant clones were selected from a mixed population during treatment. Almost all JQ1-treated parental cells had the JQ1 treatment signature in both cell lines. In contrast, JQ1-treated BBDI-resistant cells showed striking differences in the distribution of cellular identities between SUM149R and SUM159R cells. Although only 13% of cells changed their identity to the JQ1-treated type in the SUM149R cell line, nearly 50% of SUM159R cells were classified as the JQ1-treated type after JQ1 treatment (Figure 7E). Although this shift was not directly associated with the two distinct clusters identified in SUM159R cells, these observations suggest that SUM159R cells are more heterogeneous than the SUM149R line, and almost 50% of the cells still demonstrate a transcriptional response to JQ1 even though the cells continue to proliferate in the presence of the drug.

To further interrogate mechanisms of BBDI resistance in the two cell lines, we carried out a cellular barcoding experiment using the ClonTracer barcode library (Bhang et al., 2015). We cultured four replicates of barcoded SUM149 and SUM159 cells with comparable starting barcode representations in the presence of JQ1 until resistance was achieved to distinguish pre-existing clones selected during treatment from acquired alterations. We observed very different patterns of barcode selection between SUM149 and SUM159 cells. JQ1 treatment significantly reduced barcode complexity in SUM149 cells, and more than 94% of barcodes were shared by all four replicates (Figures 7F, 7G, and S7E). These findings strongly suggest that the vast majority of JQ1-resistant clones were pre-existing in the parental SUM149 cell population and highly selected for during treatment. In contrast, in SUM159 cells, there was minimal selection during JQ1 treatment because the barcode pool of the JQ1-resistant population was not significantly different from DMSO-treated parental cells at the same passage (Figures 7F, 7G, and S7E), suggesting that resistance to JQ1 in SUM159 cells is not likely due to selection for pre-existing resistant cells but acquired during treatment. These results suggest distinct patterns of JQ1 response and resistance mechanisms in TNBC.

DISCUSSION

We previously described BBDIs as candidate therapeutic agents in TNBC and also showed that acquired resistance develops

Figure 7. Single-Cell Profiling of Drug-Resistant Cells

(A and B) *t*-SNE plots depicting single cells by scRNA-seq in populations of JQ1-treated and untreated SUM149 and SUM159 parental and BBDI-resistant SUM149R and SUM159R cells, colored by cell line and treatment group (A) and by gene expression cluster (B).

(C) Top process networks enriched in differentially expressed genes between clusters 6 and 9 (DMSO) and between clusters 2 and 8 (JQ1) within SUM159R cells.

(D) *t*-SNE plots depicting single cells by scATAC-seq in populations of JQ1-treated and untreated SUM159 parental and BBDI-resistant SUM159R cells.

(E) Hexagonal plots depicting bootstrap classification of single cells in populations of parental, JQ1-treated, BBDI-resistant, and JQ1-treated BBDI-resistant cells. Each point represents a single cell and is positioned along axes according to its bootstrapping classification score for the indicated cell identity. Black, blue, and red cells are classified as parental, JQ1-treated, and BBDI-resistant cells, respectively, and gray cells are unclassified.

(F) Bar graphs show percentages of total barcodes shared among all replicates in JQ1-treated SUM149 and SUM159 cells.

(G) Pie charts show percentages of shared barcodes overlapping between untreated and JQ1-treated SUM149 and SUM159 cells.

See also Figure S7 and Table S6.

quickly, necessitating combination therapies (Shu et al., 2016). Here we describe a multi-omics profiling and functional screening approach in TNBC for identification of synthetic lethal and resistance interactions with JQ1. The advantage of this combined approach is the high confidence in the data when the same genes and pathways are identified using multiple different unbiased approaches. We identified several genes and pathways that make TNBCs more responsive or resistant to JQ1, which can be grouped into five general functional categories.

The first category encompasses chromatin modifiers and transcriptional regulators, including BBD proteins that are direct targets of JQ1 itself. Deletion of *BRD2* sensitized parental and BBDI-resistant cell lines to JQ1. Based on our data, BRD2 and BRD4 play largely overlapping roles in TNBC, but they differ in the JQ1 sensitivity of their chromatin binding. Because BRD2 is less efficiently removed from chromatin by JQ1 than BRD4, and JQ1 induces BRD2 expression, deletion of BRD2 significantly synergized with JQ1 treatment. Deletion of genes encoding multiple different Mediator proteins (*MED1*, *MED19*, and *MED24*) and *EP300* also increased sensitivity to JQ1, likely because of their direct effects on the assembly and recruitment of transcriptional complexes to active promoters. In contrast, loss of components of the BAF chromatin remodeling complex (*BRD7*, *ARID1A*, and *PBRM1*) significantly increased resistance to JQ1 of parental and BBDI-resistant cells, whereas deletion of *BRD9* increased the JQ1 sensitivity of all four cell lines. Somatic mutations of *ARID1A*, *CTCF*, *SMARCA4*, and *PBRM1* are detected at low (1%–5%) frequencies in treatment-naive breast cancers, whereas *ARID1A* mutations are more common in treatment-resistant distant metastases (Zehir et al., 2017) and in metaplastic breast cancer (Ng et al., 2017). These results suggest that alterations of the BAF complex may, in general, be associated with therapeutic resistance and perturbed differentiation.

The second category comprises regulators of protein stability and degradation, some of which may regulate the stability of BRD4 and other BBD proteins. Deletion of ubiquitination-related genes (e.g., *SPOP*, *UBE2M*, *CUL3*, and *USP14*) resulted in resistance to JQ1. SPOP is a regulator of ubiquitination-mediated degradation of BRD4 and other BBD proteins, and *SPOP* mutations in prostate cancer have been associated with BBDI resistance (Dai et al., 2017; Janouskova et al., 2017; Zhang et al., 2017). Our data are consistent with these observations and further expand the role of these proteins as regulators of BBDI sensitivity in TNBC.

The third category involves kinase signaling pathways. Deletion of *TGFBR1*, *TGFBR2*, *PIK3CA*, *EGFR*, and *TEAD1* increases JQ1 responsiveness. Small-molecule inhibitors blocking AXL, BCR-ABL, EGFR, JAK-STAT, IGFR-1, SRC, VEGFR, MEK, PIK3-AKT-mTOR, and YAP-TAZ also sensitized cells to JQ1. The effect of these signaling pathways was not always observed in all cell lines. However, *AXL* and *TEAD1* were CRISPR synergy hits in all four cell lines, and they were also validated by SMIs. Consistent with our findings, a recent study reported that BRD4 is a mediator of transcriptional addiction to YAP-TAZ in colorectal cancer and described synthetic lethal interactions between BRD4 and YAP (Zanconato et al., 2018). Similarly, BBDIs have been shown to be able to overcome cetuximab resistance in head and neck squamous cell carcinoma with activated AXL (Leonard et al., 2018).

The fourth group of genes and the compounds targeting them comprises regulators of apoptosis, including *BCL2* and *BCL2L1* (BCL-XL), which is consistent with our prior data (Shu et al., 2016). Although we validated the synergy between JQ1 and BCL2 and BCL-XL inhibitors *in vitro* and *in vivo*, the toxicity of some of these compounds (especially dual BCL2 and BCL-XL inhibitors) limits their potential for clinical development.

The fifth and the largest category includes cell cycle regulators and genes involved in DNA repair. Genetic deletion or pharmacologic inhibition of promoters of G1-S transition, including CDK4, CDK6, CCND1, SKP2, and CDK2, synergized with JQ1, whereas inactivation of genes encoding the negative regulators *CDKN1A*, *CDKN1B*, and *RB1* had the opposite effect, leading to JQ1 resistance. Multiple mechanisms could explain the synergy between JQ1 and CDK4 and CDK6 inhibitors. The mRNA and protein levels of CDK4, CCND1, and SKP2 are increased after JQ1 treatment in BBDI-resistant cells, leading to higher CDK4 kinase activity. CDK4 also regulates BRD4 protein levels via phosphorylation of SPOP and DUB3, which play a role in BRD4 ubiquitination and degradation (Dai et al., 2017; Janouskova et al., 2017; Jin et al., 2018; Zhang et al., 2017). Our data showing decreased BRD4 after palbociclib treatment imply this regulatory loop in TNBC and could explain the JQ1 CDK4 inhibition synergy in $RB1^{null}$ cells.

Although the interaction of regulators of G1 phase progression with JQ1 was largely expected because JQ1 causes G1 arrest and most transcription occurs in G1, we also identified synthetic lethal interactions between JQ1 and proteins involved in G2-M phase. Deletion of *BUB3*, inhibitors of PLK1 and AURKA kinases, and chemotherapeutic agents targeting microtubules, such as paclitaxel and vincristine, all demonstrated potent synergy with JQ1 in parental and BBDI-resistant cell lines. Deletion of DNA repair genes (e.g., *BRCA1* and *BRCA2*) and topoisomerase inhibitors sensitize TNBC cells to JQ1. BBDIs suppress DNA repair, and BET inhibition sensitizes homologous recombination-proficient tumors to PARP inhibitors (Karakashev et al., 2017; Yang et al., 2017), suggesting that breast tumors with *BRCA1* or *BRCA2* mutations may be particularly sensitive to BBDIs.

In summary, our data highlight the heterogeneity of cellular responses and resistance to JQ1 in TNBC and identify several promising combination therapies with BBDIs that could be used for the more effective treatment of chemotherapy-resistant TNBC.

STAR★METHODS

Detailed methods are provided in the online version of this paper and include the following:

- KEY RESOURCES TABLE
- RESOURCE AVAILABILITY
  - Lead Contact
  - Materials Availability
  - Data and Code Availability
- EXPERIMENTAL MODEL AND SUBJECT DETAILS
  - Breast cancer cell lines

SUPPLEMENTAL INFORMATION

Supplemental Information can be found online at https://doi.org/10.1016/j.molcel.2020.04.027.

ACKNOWLEDGMENTS

We thank members of our laboratories for critical reading of this manuscript and useful discussions. We thank the Dana-Farber Cancer Institute Molecular Biology Core Facility for outstanding sequencing service. We thank Dr. Doris Tabassum for her assistance with the dBET6 xenograft studies. This research was supported by National Cancer Institute PSOC U54 CA193461 (to F.M. and K.P.), F30 CA228208 (to J.Y.G.), R35 CA197623 (to K.P.), P01 CA080111 (to K.P. and M.B.), and SPORE P50 CA168504 (to K.P.); the Susan G. Komen Foundation (to S. Shu); and the Ludwig Center at Harvard (to K.P., F.M., M.B., and J.S.B.).

AUTHOR CONTRIBUTIONS

S. Shu performed ChIP-seq, RNA-seq, cell culture, barcoding, CRISPR, RPPA, and xenograft experiments. J.Y.G. performed synergy and xenograft studies with help from J.A. R.Z. completed dBET6 experiments with help from J.R. I.S.H. and J.E.E. performed SMI screens. C.S.R.C., E.K.P., and C.D. conducted RIME analyses. K.H. and B.M. helped with BRD7 ChIP-seq. B.J. and K.M. helped with cell culture, ChIP, immunoblots, and immunofluorescence. S. Syamala performed ChIP. A.L. ran scRNA-seq. K.L., A.F.-T., and P.C. performed ATAC-seq and scATAC-seq experiments. Q.-D.N. and R.J.M. performed xenograft experiments. H.-J.W., J.Y.G., I.S.H., X.Q., B.W., W.L., T.X., J.R., and T.O.M. completed data analyses and software development. K.W.W., J.Q., J.B., H.L., X.S.L., J.S.C., J.D.J., J.S.B., C.K., and M.B. provided reagents and resources. K.P. and F.M. supervised the study. K.P. was responsible for the overall project and the experimental part. F.M. supervised the computational analyses. All authors helped to design the study and write the manuscript.

DECLARATION OF INTERESTS

M.B. and K.P. received research support and were consultants to the Novartis Institutes for BioMedical Research during the execution of this study. K.P. serves on the scientific advisory board of Farcast Biosciences and Acrivon Therapeutics. M.B. receives sponsored research support from Novartis, serves on the SAB of Kronos Bio, and is a consultant to GTx, Inc., Aleta Biotherapeutics, and H3 Biomedicine. R.Z. and J.B. are current employees of C4 Therapeutics Inc. and Novartis, respectively. C.K. is a scientific founder, fiduciary board of directors member, scientific advisory board member, consultant, and shareholder of Foghorn Therapeutics, Inc. (Cambridge, MA). S. Shu, K.P., and J.B. are inventors of a patent on BET inhibitor resistance that DFCI licensed to Roche.

Received: November 25, 2019
Revised: March 11, 2020
Accepted: April 22, 2020
Published: May 15, 2020

REFERENCES

Abraham, J., Coleman, R., Elias, A., Holmes, F.A., Kalinsky, K., Kittaneh, M., Lower, E., Mahtani, R., Terry Mamounas, E., Pegram, M., and Vogel, C.; Breast Cancer Therapy Expert Group (BCTEG) (2018). Use of cyclin-dependent kinase (CDK) 4/6 inhibitors for hormone receptor-positive, human epidermal growth factor receptor 2-negative, metastatic breast cancer: a roundtable discussion by The Breast Cancer Therapy Expert Group (BCTEG). Breast Cancer Res. Treat. *171*, 11–20.

Anders, S., Pyl, P.T., and Huber, W. (2015). HTSeq–a Python framework to work with high-throughput sequencing data. Bioinformatics *31*, 166–169.

Benjamini, Y., and Hochberg, Y. (1995). Controlling the False Discovery Rate: A Practical and Powerful Approach to Multiple Testing. Journal of the Royal Statistical Society *57*, 289–300.

Bhang, H.E., Ruddy, D.A., Krishnamurthy Radhakrishna, V., Caushi, J.X., Zhao, R., Hims, M.M., Singh, A.P., Kao, I., Rakiec, D., Shaw, P., et al. (2015). Studying clonal dynamics in response to cancer therapy using high-complexity barcoding. Nat. Med. *21*, 440–448.

Buenrostro, J.D., Wu, B., Litzenburger, U.M., Ruff, D., Gonzales, M.L., Snyder, M.P., Chang, H.Y., and Greenleaf, W.J. (2015). Single-cell chromatin accessibility reveals principles of regulatory variation. Nature *523*, 486–490.

Cancer Genome Atlas Network (2012). Comprehensive molecular portraits of human breast tumours. Nature *490*, 61–70.

Chapuy, B., McKeown, M.R., Lin, C.Y., Monti, S., Roemer, M.G., Qi, J., Rahl, P.B., Sun, H.H., Yeda, K.T., Doench, J.G., et al. (2013). Discovery and characterization of super-enhancer-associated dependencies in diffuse large B cell lymphoma. Cancer Cell *24*, 777–790.

Chen, C.H., Xiao, T., Xu, H., Jiang, P., Meyer, C.A., Li, W., Brown, M., and Liu, X.S. (2018). Improved design and analysis of CRISPR knockout screens. Bioinformatics *34*, 4095–4101.

Cheung, K.L., Zhang, F., Jaganathan, A., Sharma, R., Zhang, Q., Konuma, T., Shen, T., Lee, J.Y., Ren, C., Chen, C.H., et al. (2017). Distinct Roles of Brd2 and

Brd4 in Potentiating the Transcriptional Program for Th17 Cell Differentiation. Mol. Cell *65*, 1068–1080.e5.

Chou, T.C., and Talalay, P. (1984). Quantitative analysis of dose-effect relationships: the combined effects of multiple drugs or enzyme inhibitors. Adv. Enzyme Regul. *22*, 27–55.

Corces, M.R., Trevino, A.E., Hamilton, E.G., Greenside, P.G., Sinnott-Armstrong, N.A., Vesuna, S., Satpathy, A.T., Rubin, A.J., Montine, K.S., Wu, B., et al. (2017). An improved ATAC-seq protocol reduces background and enables interrogation of frozen tissues. Nat. Methods *14*, 959–962.

Creech, A.L., Taylor, J.E., Maier, V.K., Wu, X., Feeney, C.M., Udeshi, N.D., Peach, S.E., Boehm, J.S., Lee, J.T., Carr, S.A., and Jaffe, J.D. (2015). Building the Connectivity Map of epigenetics: chromatin profiling by quantitative targeted mass spectrometry. Methods *72*, 57–64.

Dai, X., Gan, W., Li, X., Wang, S., Zhang, W., Huang, L., Liu, S., Zhong, Q., Guo, J., Zhang, J., et al. (2017). Prostate cancer-associated SPOP mutations confer resistance to BET inhibitors through stabilization of BRD4. Nat. Med. *23*, 1063–1071.

Delmore, J.E., Issa, G.C., Lemieux, M.E., Rahl, P.B., Shi, J., Jacobs, H.M., Kastritis, E., Gilpatrick, T., Paranal, R.M., Qi, J., et al. (2011). BET bromodomain inhibition as a therapeutic strategy to target c-Myc. Cell *146*, 904–917.

Du, P., Zhang, X., Huang, C.C., Jafari, N., Kibbe, W.A., Hou, L., and Lin, S.M. (2010). Comparison of Beta-value and M-value methods for quantifying methylation levels by microarray analysis. BMC Bioinformatics *11*, 587.

Filippakopoulos, P., Qi, J., Picaud, S., Shen, Y., Smith, W.B., Fedorov, O., Morse, E.M., Keates, T., Hickman, T.T., Felletar, I., et al. (2010). Selective inhibition of BET bromodomains. Nature *468*, 1067–1073.

Garrido-Castro, A.C., Lin, N.U., and Polyak, K. (2019). Insights into Molecular Classifications of Triple-Negative Breast Cancer: Improving Patient Selection for Treatment. Cancer Discov. *9*, 176–198.

Harris, I.S., Endress, J.E., Coloff, J.L., Selfors, L.M., McBrayer, S.K., Rosenbluth, J.M., Takahashi, N., Dhakal, S., Koduri, V., Oser, M.G., et al. (2019). Deubiquitinases Maintain Protein Homeostasis and Survival of Cancer Cells upon Glutathione Depletion. Cell Metab. *29*, 1166–1181.e6.

Hinohara, K., Wu, H.J., Vigneau, S., McDonald, T.O., Igarashi, K.J., Yamamoto, K.N., Madsen, T., Fassl, A., Egri, S.B., Papanastasiou, M., et al. (2018). KDM5 Histone Demethylase Activity Links Cellular Transcriptomic Heterogeneity to Therapeutic Resistance. Cancer Cell *34*, 939–953 e9.

Hnisz, D., Abraham, B.J., Lee, T.I., Lau, A., Saint-André, V., Sigova, A.A., Hoke, H.A., and Young, R.A. (2013). Super-enhancers in the control of cell identity and disease. Cell *155*, 934–947.

Hsu, S.C., Gilgenast, T.G., Bartman, C.R., Edwards, C.R., Stonestrom, A.J., Huang, P., Emerson, D.J., Evans, P., Werner, M.T., Keller, C.A., et al. (2017). The BET Protein BRD2 Cooperates with CTCF to Enforce Transcriptional and Architectural Boundaries. Mol. Cell *66*, 102–116.e7.

Janouskova, H., El Tekle, G., Bellini, E., Udeshi, N.D., Rinaldi, A., Ulbricht, A., Bernasocchi, T., Civenni, G., Losa, M., Svinkina, T., et al. (2017). Opposing effects of cancer-type-specific SPOP mutants on BET protein degradation and sensitivity to BET inhibitors. Nat. Med. *23*, 1046–1054.

Jeselsohn, R., Bergholz, J.S., Pun, M., Cornwell, M., Liu, W., Nardone, A., Xiao, T., Li, W., Qiu, X., Buchwalter, G., et al. (2018). Allele-Specific Chromatin Recruitment and Therapeutic Vulnerabilities of ESR1 Activating Mutations. Cancer Cell *33*, 173–186.e5.

Jin, X., Yan, Y., Wang, D., Ding, D., Ma, T., Ye, Z., Jimenez, R., Wang, L., Wu, H., and Huang, H. (2018). DUB3 Promotes BET Inhibitor Resistance and Cancer Progression by Deubiquitinating BRD4. Mol. Cell *71*, 592–605.e4.

Karakashev, S., Zhu, H., Yokoyama, Y., Zhao, B., Fatkhutdinov, N., Kossenkov, A.V., Wilson, A.J., Simpkins, F., Speicher, D., Khabele, D., et al. (2017). BET Bromodomain Inhibition Synergizes with PARP Inhibitor in Epithelial Ovarian Cancer. Cell Rep. *21*, 3398–3405.

Kim, D., Pertea, G., Trapnell, C., Pimentel, H., Kelley, R., and Salzberg, S.L. (2013). TopHat2: accurate alignment of transcriptomes in the presence of insertions, deletions and gene fusions. Genome Biol. *14*, R36.

Lambert, J.P., Picaud, S., Fujisawa, T., Hou, H., Savitsky, P., Uuskula-Reimand, L., Gupta, G.D., Abdouni, H., Lin, Z.Y., Tucholska, M., et al. (2019). Interactome Rewiring Following Pharmacological Targeting of BET Bromodomains. Mol. Cell *73*, 621–638.e17.

Leonard, B., Brand, T.M., O'Keefe, R.A., Lee, E.D., Zeng, Y., Kemmer, J.D., Li, H., Grandis, J.R., and Bhola, N.E. (2018). BET Inhibition Overcomes Receptor Tyrosine Kinase-Mediated Cetuximab Resistance in HNSCC. Cancer Res. *78*, 4331–4343.

Li, H., and Durbin, R. (2009). Fast and accurate short read alignment with Burrows-Wheeler transform. Bioinformatics *25*, 1754–1760.

Li, H., Handsaker, B., Wysoker, A., Fennell, T., Ruan, J., Homer, N., Marth, G., Abecasis, G., and Durbin, R.; 1000 Genome Project Data Processing Subgroup (2009). The Sequence Alignment/Map format and SAMtools. Bioinformatics *25*, 2078–2079.

Li, W., Xu, H., Xiao, T., Cong, L., Love, M.I., Zhang, F., Irizarry, R.A., Liu, J.S., Brown, M., and Liu, X.S. (2014). MAGeCK enables robust identification of essential genes from genome-scale CRISPR/Cas9 knockout screens. Genome Biol. *15*, 554.

Li, W., Köster, J., Xu, H., Chen, C.H., Xiao, T., Liu, J.S., Brown, M., and Liu, X.S. (2015). Quality control, modeling, and visualization of CRISPR screens with MAGeCK-VISPR. Genome Biol. *16*, 281.

Love, M.I., Huber, W., and Anders, S. (2014). Moderated estimation of fold change and dispersion for RNA-seq data with DESeq2. Genome Biol. *15*, 550.

Lovén, J., Hoke, H.A., Lin, C.Y., Lau, A., Orlando, D.A., Vakoc, C.R., Bradner, J.E., Lee, T.I., and Young, R.A. (2013). Selective inhibition of tumor oncogenes by disruption of super-enhancers. Cell *153*, 320–334.

Lun, A.T., Bach, K., and Marioni, J.C. (2016). Pooling across cells to normalize single-cell RNA sequencing data with many zero counts. Genome Biol. *17*, 75.

Mohammed, H., D'Santos, C., Serandour, A.A., Ali, H.R., Brown, G.D., Atkins, A., Rueda, O.M., Holmes, K.A., Theodorou, V., Robinson, J.L., et al. (2013). Endogenous purification reveals GREB1 as a key estrogen receptor regulatory factor. Cell Rep. *3*, 342–349.

Nagarajan, S., Rao, S.V., Sutton, J., Cheeseman, D., Dunn, S., Papachristou, E.K., Prada, J.G., Couturier, D.L., Kumar, S., Kishore, K., et al. (2020). ARID1A influences HDAC1/BRD4 activity, intrinsic proliferative capacity and breast cancer treatment response. Nat. Genet. *52*, 187–197.

Ng, C.K.Y., Piscuoglio, S., Geyer, F.C., Burke, K.A., Pareja, F., Eberle, C.A., Lim, R.S., Natrajan, R., Riaz, N., Mariani, O., et al. (2017). The Landscape of Somatic Genetic Alterations in Metaplastic Breast Carcinomas. Clin. Cancer Res. *23*, 3859–3870.

Nikolsky, Y., Ekins, S., Nikolskaya, T., and Bugrim, A. (2005). A novel method for generation of signature networks as biomarkers from complex high throughput data. Toxicol. Lett. *158*, 20–29.

O'Dwyer, P.J., Piha-Paul, S., French, C., Harward, S., Ferron-Brady, G., Wu, Y., Barbash, O., Wyce, A., Annan, M., Horner, T., et al. (2016). GSK525762, a selective bromodomain (BRD) and extra terminal protein (BET) inhibitor: results from part 1 of a phase I/II open-label single-agent study in patients with NUT midline carcinoma (NMC) and other cancers. Cancer Res. *76*, CT014.

Papachristou, E.K., Kishore, K., Holding, A.N., Harvey, K., Roumeliotis, T.I., Chilamakuri, C.S.R., Omarjee, S., Chia, K.M., Swarbrick, A., Lim, E., et al. (2018). A quantitative mass spectrometry-based approach to monitor the dynamics of endogenous chromatin-associated protein complexes. Nat. Commun. *9*, 2311.

Puissant, A., Frumm, S.M., Alexe, G., Bassil, C.F., Qi, J., Chanthery, Y.H., Nekritz, E.A., Zeid, R., Gustafson, W.C., Greninger, P., et al. (2013). Targeting MYCN in neuroblastoma by BET bromodomain inhibition. Cancer Discov. *3*, 308–323.

Qin, Q., Mei, S., Wu, Q., Sun, H., Li, L., Taing, L., Chen, S., Li, F., Liu, T., Zang, C., et al. (2016). ChiLin: a comprehensive ChIP-seq and DNase-seq quality control and analysis pipeline. BMC Bioinformatics *17*, 404.

Ramírez, F., Ryan, D.P., Grüning, B., Bhardwaj, V., Kilpert, F., Richter, A.S., Heyne, S., Dündar, F., and Manke, T. (2016). deepTools2: a next generation

web server for deep-sequencing data analysis. Nucleic Acids Res. *44* (W1), W160-5.

Ritchie, M.E., Phipson, B., Wu, D., Hu, Y., Law, C.W., Shi, W., and Smyth, G.K. (2015). limma powers differential expression analyses for RNA-sequencing and microarray studies. Nucleic Acids Res. *43*, e47.

Sanjana, N.E., Shalem, O., and Zhang, F. (2014). Improved vectors and genome-wide libraries for CRISPR screening. Nat. Methods *11*, 783–784.

Shapiro, G.I., Dowlati, A., LoRusso, P.M., Eder, J.P., Anderson, A., Do, K.T., Kagey, M.H., Sirard, C., Bradner, J.E., and Landau, S.B. (2015). Clinical efficacy of the BET bromodomain inhibitor TEN-010 in an open-label substudy with patients with documented NUT-midline carcinoma. Mol. Cancer Ther. *14*, A49.

Shu, S., and Polyak, K. (2016). BET Bromodomain Proteins as Cancer Therapeutic Targets. Cold Spring Harb. Symp. Quant. Biol. *81*, 123–129.

Shu, S., Lin, C.Y., He, H.H., Witwicki, R.M., Tabassum, D.P., Roberts, J.M., Janiszewska, M., Huh, S.J., Liang, Y., Ryan, J., et al. (2016). Response and resistance to BET bromodomain inhibitors in triple-negative breast cancer. Nature *529*, 413–417.

Tibes, R., Qiu, Y., Lu, Y., Hennessy, B., Andreeff, M., Mills, G.B., and Kornblau, S.M. (2006). Reverse phase protein array: validation of a novel proteomic technology and utility for analysis of primary leukemia specimens and hematopoietic stem cells. Mol. Cancer Ther. *5*, 2512–2521.

Tsherniak, A., Vazquez, F., Montgomery, P.G., Weir, B.A., Kryukov, G., Cowley, G.S., Gill, S., Harrington, W.F., Pantel, S., Krill-Burger, J.M., et al. (2017). Defining a Cancer Dependency Map. Cell *170*, 564–576.e16.

Whyte, W.A., Orlando, D.A., Hnisz, D., Abraham, B.J., Lin, C.Y., Kagey, M.H., Rahl, P.B., Lee, T.I., and Young, R.A. (2013). Master transcription factors and mediator establish super-enhancers at key cell identity genes. Cell *153*, 307–319.

Winter, G.E., Buckley, D.L., Paulk, J., Roberts, J.M., Souza, A., Dhe-Paganon, S., and Bradner, J.E. (2015). DRUG DEVELOPMENT. Phthalimide conjugation as a strategy for in vivo target protein degradation. Science *348*, 1376–1381.

Winter, G.E., Mayer, A., Buckley, D.L., Erb, M.A., Roderick, J.E., Vittori, S., Reyes, J.M., di Iulio, J., Souza, A., Ott, C.J., et al. (2017). BET Bromodomain Proteins Function as Master Transcription Elongation Factors Independent of CDK9 Recruitment. Mol. Cell *67*, 5–18.e19.

Wu, S.Y., Lee, A.Y., Lai, H.T., Zhang, H., and Chiang, C.M. (2013). Phospho switch triggers Brd4 chromatin binding and activator recruitment for gene-specific targeting. Mol. Cell *49*, 843–857.

Xu, G., Chhangawala, S., Cocco, E., Razavi, P., Cai, Y., Otto, J.E., Ferrando, L., Selenica, P., Ladewig, E., Chan, C., et al. (2020). ARID1A determines luminal identity and therapeutic response in estrogen-receptor-positive breast cancer. Nat. Genet. *52*, 198–207.

Yang, L., Zhang, Y., Shan, W., Hu, Z., Yuan, J., Pi, J., Wang, Y., Fan, L., Tang, Z., Li, C., et al. (2017). Repression of BET activity sensitizes homologous recombination-proficient cancers to PARP inhibition. Sci. Transl. Med. *9*, eaal1645.

Zanconato, F., Battilana, G., Forcato, M., Filippi, L., Azzolin, L., Manfrin, A., Quaranta, E., Di Biagio, D., Sigismondo, G., Guzzardo, V., et al. (2018). Transcriptional addiction in cancer cells is mediated by YAP/TAZ through BRD4. Nat. Med. *24*, 1599–1610.

Zehir, A., Benayed, R., Shah, R.H., Syed, A., Middha, S., Kim, H.R., Srinivasan, P., Gao, J., Chakravarty, D., Devlin, S.M., et al. (2017). Mutational landscape of metastatic cancer revealed from prospective clinical sequencing of 10,000 patients. Nat. Med. *23*, 703–713.

Zhang, J.H., Chung, T.D., and Oldenburg, K.R. (1999). A Simple Statistical Parameter for Use in Evaluation and Validation of High Throughput Screening Assays. J. Biomol. Screen. *4*, 67–73.

Zhang, Y., Liu, T., Meyer, C.A., Eeckhoute, J., Johnson, D.S., Bernstein, B.E., Nusbaum, C., Myers, R.M., Brown, M., Li, W., and Liu, X.S. (2008). Model-based analysis of ChIP-Seq (MACS). Genome Biol. *9*, R137.

Zhang, P., Wang, D., Zhao, Y., Ren, S., Gao, K., Ye, Z., Wang, S., Pan, C.W., Zhu, Y., Yan, Y., et al. (2017). Intrinsic BET inhibitor resistance in SPOP-mutated prostate cancer is mediated by BET protein stabilization and AKT-mTORC1 activation. Nat. Med. *23*, 1055–1062.

STAR★METHODS

KEY RESOURCES TABLE

REAGENT or RESOURCE	SOURCE	IDENTIFIER
Antibodies		
Rabbit polyclonal anti-BRD4	Bethyl laboratories	Cat# A301-985A; RRID:AB_1576498
Rabbit monoclonal anti- BRD2	Cell Signaling Technology	Cat# 5848; RRID:AB_10835146
Rabbit monoclonal anti- BRD7	Cell Signaling Technology	Cat# 14910;
Mouse monoclonal anti-H3K4me3	Abcam	Cat# ab1012; RRID: AB_442796
Rabbit Anti-Histone H3, Trimethyl (Lys27) Monoclonal Antibody,	Cell Signaling Technology	Cat# 9733, RRID:AB_2616029
Rabbit monoclonal anti- RB	Cell Signaling Technology	Cat# 9313; RRID:AB_1904119
Rabbit monoclonal anti- CCND1	Cell Signaling Technology	Cat# 2978; RRID:AB_2259616
Rabbit monoclonal anti- CDK4	Cell Signaling Technology	Cat# 12790; RRID:AB_2631166
Mouse monoclonal anti-beta-Actin	Sigma-Aldrich	Cat# A2228; RRID: AB_476697
Rabbit polyclonal anti-H3K27Ac	Abcam	Cat# ab4729; RRID: AB_2118291
Mouse monoclonal anti- E2F1	Cell Signaling Technology	Cat# 3742; RRID:AB_2096936
Rabbit monoclonal anti- Phospho-Rb-Ser780	Cell Signaling Technology	Cat# 3590; AB_2177182
Rabbit monoclonal anti- Phospho-Rb-Ser807/811	Cell Signaling Technology	Cat# 9308; RRID:AB_331472
Rabbit monoclonal anti- Phospho-Rb-Ser807/811	Cell Signaling Technology	Cat# 8516; RRID:AB_11178658
Rabbit monoclonal anti- cleaved Caspase-3	Cell Signaling Technology	Cat# 9664; RRID:AB_2070042
Rabbit polyclonal Phospho-Stat-3 (tyr705) antibody	Cell Signaling Technology	Cat# 9131, RRID:AB_331586
Mouse monoclonal anti- BrdU	Roche	Cat# 11170376001; RRID:AB_514483
Chemicals, Peptides, and Recombinant Proteins		
JQ1	Jun Qi (Dana-Farber Cancer Institute)	N/A
Palbociclib	MedChem Express	HY-50767A
ABT-199	Selleckchem	S8048
ABT263	Selleckchem	S1001
INC424	InCyte	N/A
Dasatinib	Selleckchem	S1021
TP-0903	Selleckchem	S7846
Paclitaxel	Dana-Farber Cancer Institute Research Pharmacy	N/A
Doxorubicin	Dana-Farber Cancer Institute Research Pharmacy	N/A
Vincristine	Sigma-Aldrich	V8879
Gemcitabine	Sigma-Aldrich	G6423
dBET series (dBET1 - dBET6)	Dennis Buckley (Dana-Farber Cancer Institute)	N/A
Flavopiridol	Selleckchem	S1230
Barasertib	Selleckchem	S1147
Target Selective Inhibitor Library	Selleckchem	L3500
Anti-cancer Compound Library	Selleckchem	L3000
Critical Commercial Assays		
ThruPLEX DNA-seq 48S Kit	RUBICON	R400427

(*Continued on next page*)

Continued

REAGENT or RESOURCE	SOURCE	IDENTIFIER
Experimental Models: Cell Lines		
SUM159 cell line	Steve Ethier (University of Michigan)	N/A
SUM149 cell line	Steve Ethier (University of Michigan)	N/A
SUM159R cell line	Shu et al., 2016	N/A
SUM149R cell line	Shu et al., 2016	N/A
SUM159 cell line, BRD2 KO	This paper	N/A
SUM159 cell line, BRD7 KO	This paper	N/A
SUM159 cell line, CDK4 KO	This paper	N/A
CAL-51 cell line	DSMZ	ACC 302
CAL-120 cell line	DSMZ	ACC 459
HCC38 cell line	ATCC	CRL-2314
HCC3153 cell line	Adi Gazdar/LBL Joe Gray	N/A
PMC42 cell line	R.Whitehead	N/A
MDA-MB-436 cell line	ATCC	HTB-130
MDA-MB-231 cell line	ATCC	HTB-26
Hs578T cell line	ATCC	HTB-126
Oligonucleotides - sgRNA targeting sequences		
BRD2-1: CTTCTCATCGTAACTCATG	This paper	N/A
BRD2-2: CCACGCAAAGACTTGCCTG	This paper	N/A
BRD7-1: CGGGCAGCTCGGGGCACGA	This paper	N/A
BRD7-2: CCTACAATGGGATCCACAG	This paper	N/A
CDK4-1: CCAGAGGATGACTGGCCTC	This paper	N/A
CDK4-2: CCTCACGAACTGTGCTGAT	This paper	N/A
Recombinant DNA		
CRISPR-V2	Sanjana et al., 2014	Addgene Cat# 52961
Plv(Exp)-Bsd-TRE-CDK4	This paper	Vector builder
Deposited Data		
All raw genomic data	GEO	GSE131102
All raw numeric data and image files	Mendeley	https://doi.org/10.17632/p4ypdxmsk5.1

RESOURCE AVAILABILITY

Lead Contact

Further information and requests for resources and reagents should be directed to and will be fulfilled by the Lead Contact Kornelia Polyak, Dana-Farber Cancer Institute, 450 Brookline Ave., SM1070B, Boston, MA 02215, USA. E-mail: kornelia_polyak@dfci.harvard.edu; tel: 617-632-2106; fax: 617-582-8490.

Materials Availability

SUM159 cell line derivatives generated by CRISPR-Cas9 (BRD7 KO, CDK4 KO, and BRD2 KO) will be made available upon request and following the execution of an MTA.

Data and Code Availability

All data needed to evaluate the conclusions in the paper are present in the paper and/or the STAR Methods. The accession number for the genomic data reported in this paper is GEO: GSE131102. This study did not generate custom code. Original data have been deposited to Mendeley Data: https://doi.org/10.17632/p4ypdxmsk5.1.

EXPERIMENTAL MODEL AND SUBJECT DETAILS

Breast cancer cell lines

Breast cancer cell lines were obtained from ATCC, DSMZ, or generously provided by Steve Ethier (SUM cell lines, University of Michigan) and cultured following the provider's recommendations except for SUM cell lines we used SUM medium (1:1 mix of

DMEME/F12 10% FBS with complete HMEC medium). The identity of the cell lines was confirmed based on STR and exome-seq analyses. Cells were regularly tested for mycoplasma.

Animal model

For xenograft assays female NSG (NOD.Cg-Prkdc^{scid} Il2rg^{tm1Wjl}/SzJ) and NOG (NOD.Cg-*Prkdc*^{scid} *Il2rg*^{tm1Sug}/JicTac) mice at 5-6 weeks of age were purchased from the Jackson Laboratory and Taconic, respectively. Animal experiments were performed by S.Sh. and by research technicians in the Lurie Family Imaging Center. Animal studies were performed according to protocol 11-023 or by the Lurie Family Imaging Center according to protocol 04-111, approved by the Dana-Farber Cancer Institute Animal Care and Use Committee. Mice were housed 5 to a cage with *ad libitum* access to food and water in 20°C ambient temperature, 40%–50% humidity, and 12-hour light/12-hour dark cycle.

CRISPR libraries

We used CRISPR Knock-out H1 and H2 libraries essentially as described (Jeselsohn et al., 2018).

Small molecule inhibitor libraries

The two drug libraries used for the SMI screen were the Target Selective Inhibitor Library (Catalog No.L3500) and the Anti-cancer Compound Library (Catalog No.L3000). These drug libraries were purchased from Selleck Chemicals and were compiled as previously described (Harris et al., 2019).

Barcoding and selection for resistant cells

The high-complexity barcode library, ClonTracer, was a kind gift from Frank Stegmeier (Novartis). Barcoding experiments were performed as previously described (Bhang et al., 2015). Briefly, cells were barcoded by lentiviral infection using 8 μg/ml polybrene. After a 24 h incubation with virus, infected cells were selected with 2 μg/ml puromycin. To ensure that the majority of cells were labeled with a single bar- code per cell, for lentiviral infection we used a target m.o.i. of approximately 0.1, corresponding to 10% infectivity after puromycin selection. Infected cell populations were expanded in culture for the minimal time period to obtain a sufficient number of cells to set up replicate experiments. Barcoded SUM149 and SUM159 cells were treated with increasing dose of JQ1(200nm, 500nm, 1um, 2um, 5um, and 10uM). The control groups were treated with 0.1% DMSO. Each group was cultured in quadruplicate. Cells were cultured in SUM medium. To keep the baseline control population as close as possible to that of the treatment group, each treatment group was cultured at the same passage as their corresponding control group, because random barcode loss during passaging has been reported previously. Genomic DNA was extracted from the frozen cell populations with a QIAamp DNA Mini Kit (QIAGEN). We used PCR to amplify the barcode sequence for NGS by introducing Illumina adaptors and 5-bp-long index sequences. Uniquely indexed libraries were pooled in equimolar ratios and sequenced on an Illumina NextSeq500 with single-end 75 bp reads by the Dana-Farber Cancer Institute Molecular Biology Core Facilities.

METHOD DETAILS

Xenograft assays

Animal experiments were performed by the Lurie Family Imaging Center or by our lab following protocols approved by the Dana-Farber Cancer Institute Animal Care and Use Committee. For xenograft assays 5–6-weeks old female NOD.Cg-Prkdc^{scid} Il2rg^{tm1Wjl}/SzJ and NOG (NOD.Cg-*Prkdc*^{scid} *Il2rg*^{tm1Sug}/JicTac) mice were purchased from Jackson Laboratory and Taconic, respectively. Tumors were induced by bilateral orthotopic mammary fat pad injection of 2 × 10^6 cells suspended in 50 μL of culture medium/Matrigel Growth Factor Reduced Basement Membrane Matrix, Phenol Red-Free (Corning) in a 1:1 ratio. After 14 days, mice were randomized to treatment groups based on tumor size. Mice were administered JQ1 (30 mg/kg, weekly), INC424 (75 mg/kg, daily), ABT-263 (75mg/kg, every other day per dose), ABT-199 (75mg/kg, every other day per dose), dBET6 (7.5mg/kg, daily or twice per day), palbociclib (75 mg/kg, daily), combination of JQ1 with IN424, ABT-263, ABT-199, palbociclib, or vehicle only (control) for 14 days. Tumors implanted in mice were imaged using magnetic resonance imaging (MRI) and by caliper measurement. Mice were euthanized and tumors collected, fixed overnight in 4% formalin, stored in 70% ethanol, followed by paraffin embedding, sectioning, and hematoxylin and eosin staining by the Pathology Core of the Brigham and Women's Hospital.

Immunofluorescence staining

After deparaffinization and rehydration, slides were subjected to antigen retrieval in citrate buffer pH 6 (Dako, cleaved caspase 3, BRD4, and phospho-RB) and in EDTA pH 9 buffer (Dako, pSTAT3) for 20 min in a steamer. Blocking solution (100% goat serum) was applied for 10-20 min. Incubation with primary antibody in PBS with 5% goat serum was held overnight at 4°C in a moist chamber. Secondary antibody was applied for 1 h at room temperature. Samples were mounted with VectaShield HardSet Antifade Mounting Medium with DAPI (Vector Laboratories).

Antibodies and Inhibitors

Antibodies used for ChIP-seq were BRD4 (Bethyl, A301-985A), BRD2 (Cell signaling, 5848), BRD7 (Cell Signaling, 14910), histone H3K27ac (Abcam, ab4729), histone H3K4me3 (Abcam, ab1012), and histone H3K27me3 (Cell Signaling, 9733). Antibodies used for immunoblotting were RB (Cell Signaling, 9313), CCND1 (Cell Signaling, 2978), CDK4 (Cell Signaling, 12790), E2F1 (Cell Signaling, 3742), phospho-Rb-Ser780 (Cell Signaling, 3590), phospho-Rb-Ser807/811 (Cell Signaling, 9308). Antibodies used for Immunofluorescence were BRD4 (Bethyl, A301-985A), cleaved Caspas-3 (9664), phospho-Rb-Ser807/811 (Cell Signaling, 8516), and pSTAT3 (Cell Signaling, 9131).

The JAK2 (INC424), Bcl-2 (ABT-199, S8048), and Bcl-xl/Bcl-2 (ABT263, S1001) inhibitors were from Selleckchem. The CDK4/6 inhibitor (palbociclib, HY-50767A) was from MedChemExpress. The dBET series (dBET1 - dBET10) was synthesized by Dr. Dennis Buckley (Dana Farber Cancer Institute). JQ1 was synthesized by Dr. Jun Qi (Dana Farber Cancer Institute).

Small molecule inhibitor (SMI) screens

The two drug libraries used for the SMI screen were the Target Selective Inhibitor Library (Catalog No.L3500) and the Anti-cancer Compound Library (Catalog No.L3000). These drug libraries were purchased from Selleck Chemicals and were compiled as previously described (Harris et al., 2019). Parental and BBDI-resistant (R) SUM149 and SUM159 cells were cultured DMEM/F-12 media (Life Technologies #11330057) with mammary epithelial cell growth medium supplement, 5% FBS and 1% penicillin/streptomycin until cells were seeded for screening, where RPMI 1640 media (Life Technologies #11875119) with 5% FBS and 1% penicillin/streptomycin was used. Additionally, SUM149R and SUM159R cells were cultured in the presence of 10 μM and 20 μM JQ-1, respectively, until the cells were seeded for screening, after which JQ-1 was not included in media. For the SMI screen, 500 cells per well for SUM149/SUM149R cells and 250 cells per well for SUM159/SUM159R were seeded. A Z' factor for each cell line was determined using vincristine (1 μM) as a cytotoxic agent (Zhang et al., 1999). The Z' factor for cell lines were as follows: SUM149 = 0.35; SUM149R = 0.56; SUM159 = 0.60; SUM159R = 0.38. Cells were seeded in 30 μl and after one day, 100 nL of molecules from the drug libraries were delivered by pin-transfer and 20 μl of fresh media was added. After 72 hours, plates were harvested and data was collected as previously described (Harris et al., 2019). All dose-response curves were completed in duplicate. Statistical analysis of dose-curves was completed in GraphPad Prism 8 (nonlinear regression, variable slope, four parameters, bottom constant equal to 0, top constant equal to 1). LogIC_{50} values were compared with an extra sum-of-squares F Test.

CRISPR Screen and data analyses

We used CRISPR Knock-out H1 and H2 libraries essentially as described (Jeselsohn et al., 2018). For the pooled genome-wide CRISPR screen, 200 million SUM149 and SUM159 parental and BBDI-resistant cells were infected with the pooled lentiviral CRISPR knock-out H1 and H2 library at a multiplicity of infection of 0.3 to ensure that most cells receive only one viral construct with high probability. After 5 days of puromycin selection, the surviving cells were divided into day 0 control cells and cells cultured for five passages treated with DMSO or JQ1 (500nM and 1uM for SUM159; 100nM, 200nM, 400nM, 800nM for SUM149; 20uM for SUM159R; 10uM for SUM149R cells) before genomic DNA extraction and library preparation. The CRISPR screens were also repeated in SUM159 cells with DMSO or JQ1 treatment (500nM, 1000nM). PCR was performed on genomic DNA to construct the sequencing library. Each library was sequenced at 30∼40 million reads to achieve ∼300 × average coverage over the CRISPR library. The day 0 sample library of each screen served as controls to identify positively or negatively selected genes or pathways.

Generation of Single CRISPR/Cas9 Knock-Out cells

Construction of lenti-CRISPR/Cas9 vectors targeting BRD2, BRD7, and CDK4 was performed following the protocol associated with the backbone vector lentiCRISPR V2 (Sanjana et al., 2014) (49535, Addgene). The sgRNA sequences used are listed in the Key resources table. SUM159 and SUM159R cells were infected with lentivirus expressing sgRNAs targeting *CDK4*, *BRD2,* or *BRD7*. After puromycin selection, single cell clones were picked and expanded, and knockout was verified by western blot analyses.

Generation of TET-inducible exogenous CDK4-expressing CDK4 knockout cells

SUM159 cells were infected with TET-inducible GFP-CDK4 resistant to *CDK4* sgRNA-1 virus. After blasticidin selection, three days of doxycycline treatment induces the GFP-CDK4 expression. GFP positive cells were sorted by FACS. The SUM159 inducible CDK4 positive cells were infected with *CDK4* knockout sgRNA virus for endogenous *CDK4* knockout. After puromycin selection, the cells from single cell cloning were grown and treated with or without doxycycline. CDK4 expression was confirmed by western blot.

Immunoblotting and immunoprecipitation experiments

Cells were lysed in RIPA buffer. Proteins were resolved in SDS-polyacrylamide gels (4%–12%) and transferred to PVDF membranes by using a Tris-glycine buffer system. Membranes were blocked with 5%milk powder in 0.1% Tween20 in PBS (PBS-T) for 1 hr at room temperature followed by incubation with primary antibodies at 1:1000 dilution in 2.5% milk PBS-T. For immunoprecipitation, nuclear extracts were prepared as follow: 10x 10^6cells were resuspended in 5ml Buffer A: 10mM Tris pH 7.9, 1.5mM MgCl2, 10mM KCl, 0.05% NP-40, 1mM DTT, and protease and phosphatase inhibitors. Cells were incubated on ice for 15 min and gently vortexed every 5 min. After centrifugation at 2,000 g for 5 min, pellets were suspended in 0.3 mL buffer B (20mM Tris pH 7.9, 25% glycerol, 0.42 M NaCl, 1.5mM MgCl2, 1mM KCl, 0.5% NP40, 0.2mM EDTA, 1mM DTT, and protease and phosphatase inhibitors)

and incubated for 5 min on ice. After centrifugation of the lysates at 14 g for 10 min at 4°C, supernatant was diluted with 0.6 mL buffer A, and added NP-40 to final 0.5% and treated with DNase I. The samples were then incubated at 4°C overnight with BRD4 antibody at 1:100 dilution and immunoprecipitates were collected on Dynabeads Protein G for 2 hr. Beads were washed with buffer B containing 150mM NaCl and 0.5% NP-40 three times and then resuspended in gel loading buffer.

ChIP-seq

For BRD2 and BRD4 ChIP-Seq, SUM149, SUM159, SUM149R, and SUM159R cells ($1x10^7$) were grown in SUM Medium. The media were then removed and replaced with PBS containing 1% formaldehyde (EM grade; Tebu-bio) and crosslinked for 8 min at 37°C. Crosslinking was quenched by adding glycine to a final concentration of 0.2 M. For BRD7 ChIP-Seq, SUM159 and SUM159R cells ($8x10^7$) were grown in SUM medium. For BRD4, H3K27ac, H3K4me3, and H3K27me3 ChIP-Seq SUM159 WT and BRD7 KO cells ($1x10^7$) were grown in SUM Medium. The medium was removed and replaced with PBS containing 2mM DSG (disuccinimidyl glutarate, ThermoFisher) and incubated for 30 min at room temperature, then removed and replaced with PBS containing 1% formaldehyde (EM grade; Tebu-bio) and crosslinked for 8 minutes at 37°C. Crosslinking was quenched by adding glycine to a final concentration of 0.2 M. The cells were washed with ice-cold PBS, harvested in PBS, and the cell pellet was washed with PBS. The nuclear fraction was extracted by first resuspending the pellet in 10 mL of LB1 buffer (50mM HEPES-KOH [pH 7.5], 140mMNaCl, 1mMEDTA, 10% glycerol, 0.5% NP-40 or Igepal CA-630, and 0.25% Triton X-100) for 10 min at 4°C. Cells were pelleted, resuspended in 10 mL of LB2 buffer (10 mM Tris-HCL [pH 8.0], 200 mM NaCl, 1 mM EDTA, and 0.5 mM EGTA), and mixed for 5 min. Cells were pelleted and resuspended in 1ml LB3 buffer (10 mM Tris-HCl [pH 7.4], 1 mM EDTA, 0.1%SDS, 1%Triton X-100, 0.1% Na-deoxycholate, 1Mm DTT, 0.25% N-lauroylsarcosine, protease inhibitors and phosphatase inhibitors) and sonicated in a Covaris sonicator for 10 min. A total of 30 μl of 5M NaCl was added, and lysate was centrifuged for 10 min at 20,000 *rcf.* to purify the debris. The supernatant was then incubated with 50 μl of magnetic beads (Life Technologies) prebound with 20 μg BRD4 antibody (Bethyl, A301-985A), 20 μl BRD2 antibody (Cell signaling, 5848), 40 μl BRD7 antibody (Cell Signaling, 14910) and immunoprecipitation (IP) was conducted overnight in the cold room. The beads were washed ten times in 1 mL of RIPA buffer and twice in 100mM ammonium hydrogen carbonate (AMBIC) solution. DNA was eluted in elution buffer (50 mM Tris-HCl pH 8, 10 mM EDTA, and 1% SDS). Cross-links were reversed overnight at 65°C. RNA and protein were digested with 0.2 mg/mL RNase A for 2 hr followed by 0.2 mg/mL Proteinase K for 1 hr. DNA was purified with phenol chloroform extraction and ethanol precipitation. Libraries for Illumina sequencing were prepared following the Rubicon ThruPLEX-FD kit for 10-12 cycles.

RNA-seq

SUM149 and SUM149R were incubated in biological duplicates for 12 hr with 500 nM of JQ1 or DMSO treatment. Total RNA was extracted using the standard QIAGEN RNeasy kit (74106). RNA concentrations were measured and quality controlled on a Bioanalyzer, RNA-Seq libraries were made using Illumina True-Seq RNA kits using the Sciclone NGSx workstation.

qPLEX-RIME

Samples were digested and purified with the Ultra-Micro C18 Spin Columns (Harvard Apparatus) as previously described (Papachristou et al., 2018). After purification, each sample was dried and reconstituted in 100ul 0.1M TEAB (triethylammonium bicarbonate) and labeled with the TMT-10plex reagents (Thermo Fisher). The peptide mixture was fractionated with Reversed-Phase spin columns at high pH (Pierce, #84868) and each fraction was analyzed on a Dionex Ultimate 3000 UHPLC system coupled with the LTQ Orbitrap Velos mass spectrometer (Thermo Scientific). Mobile phase A was composed of 2% acetonitrile, 0.1% formic acid, 5% dimethyl sulfoxide (DMSO) and mobile phase B was composed of 80% acetonitrile, 0.1% formic acid, 5% DMSO. The precursor scans were performed in the Orbitrap in the range of 380-1500 m/z at 60K resolution. The MS2 scans were performed in the ion trap with CID collision energy 30% and in the Orbitrap with HCD collision energy 40% back-to-back for each precursor. The raw data were processed on Proteome Discoverer 2.1 using the SequestHT search engine. The node for SequestHT included the following settings: Precursor Mass Tolerance 20ppm, Fragment Mass Tolerance 0.5Da for the CID spectra and 0.05Da for the HCD spectra, Dynamic Modifications were Oxidation of M (+15.995Da), Deamidation of N/Q (+0.984Da) and Static Modifications were TMT6plex at any N terminus/K (+229.163Da).

Mass spectrometry analysis of histone modifications

Histones were isolated from cell nuclei using acid extraction, biochemically prepared, and analyzed by mass spectrometry against a reference of stable isotope-labeled synthetic peptide standards exactly as described (Creech et al., 2015).

DNA methylation

DNA methylation profiling was carried out on Infinium HumanMethylation450K BeadChip arrays (Illumina, discontinued) at the Harvard Medical School-Partners HealthCare Center for Genetics and Genomics.

Single cell RNA-Seq

Cells were collected by trypsinization and processed according to the 10xGenomics scRNA-seq sample preparation protocol (Chromium Single Cell 3′ v2 Reagent Kit, 10xGenomics). 2,000 cells were targeted for each sample.

ATAC-Seq

50,000 cells were resuspended in 1 mL of cold ATAC-seq resuspension buffer (RSB; 10 mM Tris-HCl pH 7.4, 10 mM NaCl, and 3 mM MgCl2 in water). Cells were centrifuged at max speed for 5 min in a pre-chilled (4 C) fixed-angle centrifuge. After centrifugation supernatant was carefully aspirated. Cell pellets were then resuspended in 50 μL of ATAC-seq RSB containing 0.1% NP40, 0.1% Tween-20, and 0.01% digitonin by pipetting up and down three times. This cell lysis reaction was incubated on ice for 3 min. After lysis, 1 mL of ATAC-seq RSB containing 0.1% Tween-20 (without NP40 or digitonin) was added, and the tubes were inverted to mix. Nuclei were then centrifuged for 5 min at max speed in a pre-chilled (4 C) fixed-angle centrifuge. Supernatant was removed and nuclei were resuspended in 50 μL of transposition mix (reference to OMNI paper) 2.5 μL transposase (100 nM final), 16.5 μL PBS, 0.5 μL 1% digitonin, 0.5 μL 10% Tween-20, and 5 μL water) by pipetting up and down six times. Transposition reactions were incubated at 37 C for 30 min in a thermomixer with shaking at 1,000 rpm Reactions were cleaned up with QIAGEN columns. Libraries were amplified as described previously (Buenrostro et al., 2015).

Single cell ATAC-seq

Cells were collected by trypsinization and cryopreserved in 10% DMSO. Subsequently cells were thawed and nuclei prepared and transposed according to the OMNI-ATAC protocol (Corces et al., 2017). From that point ~2,000 cells were targeted for each sample and processed according to the 10xGenomics scATAC-seq sample preparation protocol (Chromium Single Cell ATAC Library & Gel Bead Kit, V1.0 10xGenomics).

Public data analysis

RNA-seq gene expression profile (RSEM counts) and the major breast tumor subtypes (Luminal A, Luminal B, Normal, HER2, and Basal) in the TCGA cohort were obtained from Broad GDAC Firehose database (https://gdac.broadinstitute.org/). The three TNBC subtypes were defined by using GSVA algorithm and gene expression signatures identified in our lab (B.J., unpublished data). JQ1 resistance score was defined by using GSVA algorithm on the differentially expressed genes (DEGs) between untreated and JQ1-treated cells. The intersected DEGs identified in SUM149 and SUM159 were used. Survival analyses were performed by using survminer R package (https://cran.r-project.org/web/packages/survminer/index.html). Gene co-dependency data were obtained from DepMap portal (https://depmap.org/portal/). The relationship between CRISPR screen results and gene co-dependency was studied.

QUANTIFICATION AND STATISTICAL ANALYSIS

Software used in this study

cutadapt v1.8.1, bowtie2 v2.3.3, samtools v1.9, picard v1.123, MACS2 v2.1.0.20150731, Tophat2 v2.0.11, HT-seq v0.6.1p1, DEseq2 1.22.2, BWA, GATK, MuTect v1.1.4, ROSE v0.1, Cell Ranger v2.0.2, Seurat v2, MAGeCK v0.5.7

ChIP-seq data analysis

Adaptor sequences of ChIP-seq raw reads are removed by using cutadapt (https://doi.org/10.14806/ej.17.1.200). Trimmed reads are aligned by bowtie2 using default parameters to version hg19 of human genome. The samtools (Li et al., 2009) and picard (http://broadinstitute.github.io/picard) are used to sort and remove duplicated reads to avoid PCR bias from the sequencing process. Peak calling (identification of regions of ChIP-seq enrichment over background) is performed by using MACS2 (Zhang et al., 2008) with parameters of "–extsize=146 –nomodel." Enhancers are identified from H3K27ac data in SUM149 and SUM159 by using ROSE pipeline (Hnisz et al., 2013).

RNA-seq data analysis

Raw RNA-seq reads are aligned to version hg19 of human genome by using Tophat2 (Kim et al., 2013) with the default parameters. Gene counts are quantified by using HT-seq (Anders et al., 2015) with REFSEQ annotation. Differentially expressed genes are identified by using DESeq2 (Love et al., 2014) with cutoff of q value < 0.001, ranked by the statistics.

Barcoding data analysis

We followed the method used in Bhang et al. (2015) with small modifications. In details, all sequencing reads are trimmed by using 3′ adaptor sequence: AGCAGAGCTACGCACTCTATGCTAGTGCTAGAGATCGGAAGAGCACACGTCTGAACTCCAGTCACTCACGAT CGTATCTCGTATGCCGTCTTCTGCTTG with minimum alignment length of 40-nt. The trimmed reads with Ns or less than 30-nt or without the WS x 15 pattern are removed. Then the 30-nt barcode sequences are extracted from the 3′ prime end of the trimmed sequences. Barcodes with an estimated Phred quality score of at least 10 for all nucleotides and with an average Phred quality score greater than 30 are kept as qualified barcodes. The barcodes with only one count are excluded from the analyses to avoid the noise derived from the sequencing error.

Drug synergy analysis

Synergy studies were performed in 384-well plates (Corning). SUM159 cells were seeded at a density of 200 cells/well, SUM159R and SUM149 at a density of 500 cells/well, and SUM149R, CAL-120, CAL-51, HCC38, HCC3153, Hs578-T, MDA-MB-231,

MDA-MB-436, and PMC42 at a density of 1000 cells/well, in 50 μL of media. The following day, the cells were imaged and counted using the Celigo Imaging Cytometer (Nexcelom). Drugs were then pin-transferred into the wells from a 500X concentrated drug plate made in a 384-well plate (Greiner Bio-One) using the JANUS Automated Workstation (Perkin Elmer). Five concentrations for each drug were chosen between 20% and 80% inhibition, and half doses were used for combinations (see Table S5 for list of concentration of each compound used), with 4 replicate wells for each concentration of each drug alone and 8 replicates of each concentration pair. After approximately 3 cell doublings (3 days for SUM series, CAL-51, and MDA-MB-231; 4 days for PMC42; 5 days for CAL-120, HCC3153, Hs578-T, and MDA-MB-436; and 6 days for HCC38), cells were stained with 5 μg/mL Hoechst 33342 (Sigma-Aldrich) and 2 μg/mL propidium iodide (Sigma-Aldrich) in PBS, and nuclei were imaged and counted using the Celigo Imaging Cytometer. Propidium iodide-positive dead cells were subtracted from the total Hoechst-positive nuclei to determine the number of live cells, which were then normalized to the baseline number of cells. Combination indices were determined using the median-effect principle of Chou and Talalay (1984). Isobologram plots were generated using R.

Single cell RNA-seq data analysis

Single cell RNA-seq data generated by 10x genomics were preprocessed using the Cell Ranger (https://www.10xgenomics.com/) to obtain the UMI (unique molecular identifier) counts for each gene. To get a reliable single cell transcriptome dataset, we excluded the cells with less than 200 genes expressed (UMI > 0) or the cells with more than 80% UMIs from mitochondrial genes. The filtered data were then normalized and scaled by using Seurat to remove unwanted source of variations (Lun et al., 2016). T-SNE was performed on the normalized data to visualize the single cells in two-dimensional space by using the top 10 dimensions of principal component analysis (PCA). Unsupervised clustering was performed by using ''FindClusters'' function in Seurat package with parameter of resolution = 0.8. Cell cycle phases of all single cells were assigned by using cyclone function in scran package (Lun et al., 2016). Genes with differential expression between clusters were obtained by using Wilcoxon rank-sum test. FDR was then calculated to correct for multiple testing.

Identification of pre-existing resistant cells from single cell transcriptome

Cell identity signatures of SUM149, JQ1-treated SUM149 and SUM149R cells: For each of the three cell types, we compare the bulk gene expression of it with the other two cells together. We choose the top most 100 upregulated and downregulated genes as the (up and down) signatures of the cell type. Cell identity signatures of SUM159, JQ1-treated SUM159 and SUM159R cells are obtained in the same way. Calculation of cell identity score: For each single cell, we calculated the average expression of each set of up signature genes minus the average expression of each set of down signature genes as the cell identity score. We carried out a bootstrap procedure to estimate the significance of the cell identity score. We randomly select 1,000 sets of up and down signatures with the same size of the original true signatures, generated the bootstrap distribution of the cell identity score, and calculated the bootstrap p value based on the distribution. We classified the single cells based on the bootstrap p value cutoff of 5%. If a cell did not pass the test of any signature, it is annotated as unclassified. Hexagonal plots were used to show the bootstrap classification of single cells in indicated cell populations, in which cells showed clear identity (passed the 5% threshold) are positioned on the edge of the plot.

CRISPR screen data analysis

CRISPR data were analyzed by MAGeCK and MAGeCK-VISPR essentially as described (Chen et al., 2018; Jeselsohn et al., 2018; Li et al., 2015). Briefly, raw sequencing data are pre-processed by using MAGeCK (Li et al., 2014) to obtain the read counts for each sgRNA. Control sgRNAs are used to normalize the data. MAGeCK TEST algorithm is used to compare treatment with control samples to obtain the significant enriched and depleted sgRNAs and genes. Genes with p value less than 0.001 are candidate hits. Different doses and replicates of JQ1 treatment libraries in the same cell line are tested separately and merged together by choosing the lowest p value. If one gene is enriched in one library and depleted in the other, or vice versa, the gene is set as not changed. MageckFlute package (Li et al., 2014) was used to visualize the data.

DNA methylation

DNA methylation profiling was carried out on Infinium HumanMethylation450K BeadChip arrays (Illumina, discontinued) at the Harvard Medical School-Partners HealthCare Center for Genetics and Genomics. The methylation status of the cell lines was obtained using the *Infinium HumanMethylation450 BeadChip Kit* from Illumina. The unnormalized probe-level beta-values (Du et al., 2010) of each sample were obtained from the raw data using the *Illumina GenomeStudio* software (GSGX v1.1.0). The normalization of the beta-values was performed using the R Bioconductor package *lumi*. The normalized M-value thus obtained were converted back to normalized beta-values using the following formula:

$$\text{Beta} - \text{value} = (2\hat{}\text{M} - \text{value})/\{(2\hat{}\text{M} - \text{value}) + 1\}(\text{Duetal.}, 2010)$$

The normalized beta-values of each sample were then collapsed to promoters and enhancers of genes. Briefly, each probe is attempted to be assigned to either a promoter, enhancer, or gene-body of a gene using the annotation provided in the output of the GenomeStudio software mentioned above. The methylation status of the enhancer of a gene is determined by taking the average normalized beta-values of all the probes assigned to the enhancer of that. Depending on the position of the probes relative to the

TSS of a gene, the probes are also assigned to either promoters (TSS200, TSS1500, 1stExon, and 5′UTR) or gene-body (Body, 3′UTR) of genes. Following that, single gene-level methylation values of each gene's promoter and gene-body are obtained using the average normalized beta-values as explained for enhancers. The gene-level enhancer, promoter, and gene-body methylation values of each sample have been used to determine the correlation between the samples and their tissue of origin (lineage).

ATAC-seq

ChiLin pipeline 2.0.0 (Qin et al., 2016) is used for QC and preprocess of the ATAC-seq. We use Burrows-Wheeler Aligner (BWA) (Li and Durbin, 2009) as a read mapping tool, and Model-based Analysis of ChIP-Seq (MACS2) (Zhang et al., 2008) as a peak caller, with a q-value (FDR) threshold of 0.01.Based on a dynamic Poisson distribution MACS2 can effectively capture local biases in the genome sequence, allowing for more sensitive and robust prediction of binding sites. Unique read for a position for peak calling is used to reduce false positive peaks, statically significant peaks are finally selected by calculated false discovery rate of reported peaks. Deeptools (Ramírez et al., 2016) is used for the heatmap plots. ATAC-seq peaks from all study samples were merged to create a union set of sites. Read densities were calculated for each peak for each sample, differential peaks between WT and KO were identified by DEseq2 (Love et al., 2014) with adjusted $p \leq 0.05$, $|\log2\text{fold change}| \geq 1$.

Single cell ATAC-seq

Single-cell ATAC-seq data were processed using the Cell Ranger ATAC pipeline v1.1.0, which provides QC and clustering. Any cell that had Fraction of reads in peaks (FRiP) < 0.2 and total fragments < 1,000 was removed from the analysis, total 2,701 cells passed the QC. Median fragments per cell is 27,599, fraction of transposition events in peaks is 32.8%. The t-SNE analysis was performed using the implementation from the Loupe Cell Browser 3.1.0.

Exome Sequencing

Exome sequencing was performed in the Dana-Farber Cancer Institute Center for Cancer Genome Discovery as previously described (Shu et al., 2016).

RIME

Peptide intensities were normalized using median scaling and protein level quantification was obtained by the summation of the normalized peptide intensities. A statistical analysis of differentially-regulated proteins was carried out using qPLEXanalyzer a Bioconductor R-package (Papachristou et al., 2018), which internally uses limma R-package from Bioconductor (Ritchie et al., 2015). Multiple testing correction of p values was applied using the Benjamini-Hochberg method (Benjamini and Hochberg, 1995) to control the false discovery rate.